

Joint Discriminative-Generative Modeling via Dual Adversarial Training

Xu Wang Yin
Independent
xuwangyin@gmail.com

Claire Zhang
MIT
clairefz@mit.edu

Julie Steele
MIT
jssteele@mit.edu

Nir Shavit
MIT
shanir@csail.mit.edu

Tony T. Wang
MIT
twang6@mit.edu

Abstract

Simultaneously achieving robust classification and high-fidelity generative modeling within a single framework presents a significant challenge. Hybrid approaches, such as Joint Energy-Based Models (JEM), interpret classifiers as EBMs but are often limited by the instability and poor sample quality inherent in Stochastic Gradient Langevin Dynamics (SGLD)-based training. We address these limitations by proposing a novel training framework that integrates adversarial training (AT) principles for both discriminative robustness and stable generative learning. The proposed method introduces three key innovations: (1) the replacement of SGLD-based JEM learning with a stable, AT-based approach that optimizes the energy function by discriminating between real data and Projected Gradient Descent (PGD)-generated contrastive samples using the BCE loss; (2) synergistic adversarial training for the discriminative component that enhances classification robustness while eliminating the need for explicit gradient penalties; and (3) a two-stage training strategy that addresses normalization-related instabilities and enables leveraging pretrained robust classifiers, generalizing effectively across diverse architectures. Experiments on CIFAR-10/100 and ImageNet demonstrate that our approach: (1) is the first EBM-based hybrid to scale to high-resolution datasets with high training stability, simultaneously achieving state-of-the-art discriminative and generative performance on ImageNet 256×256 ; (2) uniquely combines generative quality with adversarial robustness, enabling critical applications like robust counterfactual explanations; and (3) functions as a competitive standalone generative model, matching the generative quality of autoregressive methods (VAR-d16) and surpassing diffusion models while offering unique versatility.

1 Introduction

Deep learning models have traditionally been developed with either discriminative or generative objectives in mind, rarely excelling at both simultaneously (Ng and Jordan, 2001; Jebara, 2004; Lasserre et al., 2006; Xie et al., 2016; Grathwohl et al., 2019). Discriminative models are optimized for classification or regression tasks but lack the ability to model data distributions, while generative models can synthesize new data samples but may underperform on downstream classification tasks (Ng and Jordan, 2001; Jebara, 2004). Recent research has explored unifying these approaches through joint discriminative-generative modeling frameworks that aim to combine the predictive power of discriminative approaches with the rich data understanding of generative models (Xie et al., 2016; Lazarow et al., 2017; Jin et al., 2017; Du and Mordatch, 2019; Grathwohl et al., 2019; Chen et al., 2019; Guo et al., 2023; Deja et al., 2023).

Among these unification efforts, Energy-Based Models (EBMs) have emerged as a promising framework due to their flexibility and theoretical connections to both paradigms. In particular, Joint Energy-Based Models (JEM) (Grathwohl et al., 2019) demonstrated that standard classifier archi-

tures could be reinterpreted to simultaneously function as EBMs, enabling both high-accuracy classification and reasonable sample generation. However, a critical limitation of JEM and similar approaches is their reliance on Markov Chain Monte Carlo (MCMC) methods such as Stochastic Gradient Langevin Dynamics (SGLD) for training the generative component. SGLD-based EBM learning suffers from significant training instabilities, computational inefficiency, and often produces poor-quality samples (Grathwohl et al., 2019; Duvenaud et al., 2021; Du and Mordatch, 2019; Zhao et al., 2020; Gao et al., 2018; Nijkamp et al., 2019), limiting the practical adoption of these hybrid models.

We address these limitations by introducing **Dual Adversarial Training (DAT)**, a novel framework that leverages adversarial training (AT) principles for both discriminative robustness and stable generative learning within a unified JEM-based architecture. Our approach employs a dual application of adversarial training: (1) standard AT for the discriminative component to achieve robustness against adversarial perturbations, and (2) an AT-based energy function learning strategy for the generative component that replaces unstable SGLD-based JEM learning.

Our key technical contributions include:

1. **A stable AT-based alternative to SGLD-based JEM learning.** We replace the unstable SGLD-based JEM learning with an adversarial training approach that optimizes the energy function through Binary Cross-Entropy loss using Projected Gradient Descent (PGD; Madry et al. 2017)-generated contrastive samples. This fundamentally addresses the training instabilities that have plagued JEM, enabling reliable convergence and significantly improved sample quality.
2. **Adversarial training with synergistic effects.** We incorporate adversarial training for the discriminative component, which not only enhances classification robustness but also eliminates the need for explicit R_1 gradient penalty required by previous AT-EBMs frameworks (Yin et al., 2022), simplifying the training procedure and avoiding constraints on model expressiveness.
3. **Two-stage training strategy.** We introduce a two-stage training strategy that provides practical benefits including leveraging pretrained robust classifiers and addressing normalization-related instabilities. This strategy generalizes across diverse architectures, working effectively for both ResNet (with batch normalization) and ConvNeXt (with layer normalization).

Experiments on CIFAR-10/100 and ImageNet demonstrate the effectiveness and scalability of our approach. Notably, our approach represents the first hybrid model to achieve competitive generative quality, strong classification performance, and adversarial robustness simultaneously—establishing that hybrid models need not compromise on any dimension. This establishes three advances for hybrid modeling:

1. **First EBM-based hybrid that scales to high-resolution complex datasets.** Prior EBM-based hybrid approaches (IGEBM, JEM, SADA-JEM) could not scale beyond low resolution or achieve competitive generative performance on ImageNet-level datasets due to SGLD instability. Our approach is the first to overcome these limitations, achieving competitive generative quality and strong classification performance on ImageNet 256×256 with high training stability, demonstrating that EBM-based hybrid models can scale reliably to complex, high-resolution datasets.
2. **Generative quality and adversarial robustness for critical applications.** While other scalable hybrids like the diffusion-based EGC achieve reasonable performance, they do not reach state-of-the-art generative quality and lack adversarial robustness. Our dual capability of generative quality and adversarial robustness enables robust counterfactual explanations that are substantially more faithful to target class characteristics than non-robust or robustness-only methods (Section 4.3.2), essential for interpretable ML in high-stakes domains.
3. **Flexibility as a competitive generative model.** When evaluated purely on generation quality, our approach (with ConvNeXt-Large) matches the autoregressive model VAR-d16 and surpasses diffusion models (ADM, LDM) on ImageNet 256×256 , while achieving significantly higher throughput than diffusion models. Beyond this competitive quality, our energy-based approach offers unique versatility for diverse synthesis tasks (inpainting, super-resolution, image manipulation) and compositional generation (Du et al., 2020; Santurkar et al., 2019).

These results demonstrate that hybrid models are no longer a compromise in either generative quality or classification performance—they can match state-of-the-art specialized models in both dimensions while providing the unique capabilities described above.

2 Related work

Joint discriminative-generative modeling The pursuit of joint discriminative-generative modeling, or hybrid modeling, aims to combine the predictive power of discriminative approaches with the rich data understanding of generative models within a single framework. This line of research is motivated by the potential to improve classifier robustness, calibration, and out-of-distribution detection (Grathwohl et al., 2019; Du and Mordatch, 2019), while also enabling tasks like sample generation (e.g., for counterfactual explanation (Deja et al., 2023)) and semi-supervised learning (Kingma et al., 2014). A significant thrust in this area involves Energy-Based Models (EBMs). Early work by Xie et al. (2016) showed how generative ConvNets could be derived from discriminative ones, framing them as EBMs. Du and Mordatch (2019) demonstrated that implicitly generative EBMs can achieve strong performance on discriminative tasks like adversarially robust classification and out-of-distribution detection, while addressing scalable EBM training challenges. Grathwohl et al. (2019) introduced Joint Energy-Based Models (JEM), which explicitly reinterpret standard classifiers as EBMs over the joint distribution of data and labels $p(x, y)$, allowing simultaneous classification and generation. Yang et al. (2023) incorporated sharpness-aware minimization (SAM) to smooth energy landscapes and removed data augmentation from the EBM loss term to improve both classification accuracy and generation quality of JEM. Guo et al. (2023) proposed EGC, which employs Fisher divergence within a diffusion framework to learn an unconditional score function $\nabla \log p(x)$ and a conditional classifier $p(y|x)$ for unified classification and generation, thereby circumventing the computational challenges of traditional energy-based model training.

Alternative architectural approaches have also been explored for joint modeling. Rather than energy-based formulations, joint diffusion models (Deja et al., 2023) attach classifiers directly to diffusion model UNet encoders for joint end-to-end training. Another distinct approach is “introspective learning,” where a single model functions as both a generator and a discriminator through an iterative self-evaluation process, developed across works by Lazarow et al. (2017), Jin et al. (2017), and Lee et al. (2018). Flow-based models have also been explored for hybrid tasks; for instance, Residual Flows (Chen et al., 2019) utilized invertible ResNet and showed competitive performance in joint generative and discriminative settings, offering an alternative to EBMs by allowing exact likelihood computation. These diverse approaches underscore the continued effort to create models that synergistically leverage both discriminative and generative learning.

Joint Energy-Based Models (JEM) A significant step towards unifying discriminative and generative modeling within a single framework was presented by Grathwohl et al. (2019) with their Joint Energy-Based Model (JEM). Their key insight was to reinterpret the logits produced by a standard discriminative classifier, typically used to model $p(y|x)$, as defining an energy function for the joint distribution $p(x, y)$. Specifically, they defined the energy $E_\theta(x, y)$ as the negative of the logit corresponding to class y , $E_\theta(x, y) = -f_\theta(x)[y]$. This formulation allows for the recovery of the standard conditional distribution $p(y|x)$ via softmax normalization over y , while also yielding an unnormalized probability density $p(x)$ by marginalizing out y , effectively using the negative Log-SumExp of the logits as the energy function for $p(x)$. They proposed a hybrid training objective that combines the standard cross-entropy loss for $p(y|x)$ with an EBM-based objective for $p(x)$ optimized using Stochastic Gradient Langevin Dynamics (SGLD) (Welling and Teh, 2011). Grathwohl et al. (2019) demonstrated that this joint training approach allows JEM to achieve strong performance on both classification and generative tasks, while simultaneously improving classifier calibration, out-of-distribution detection capabilities, and robustness against adversarial examples compared to standard discriminative training.

Our work builds upon these foundations by incorporating adversarial training principles into the joint modeling framework. Our approach is motivated by the theoretical insight that adversarially robust classifiers implicitly learn energy functions (Zhu et al., 2021; Wang et al., 2022a; Mirza et al., 2024), and we draw particularly from recent advances in adversarial training for EBMs (Yin et al., 2022) and methods for achieving robustness on both in-distribution and out-of-distribution data (Augustin et al., 2020; Korst and Asadulaev, 2022). Applications of robust classifiers to image synthesis are explored by Santurkar et al. (2019), who demonstrate that robust classifiers can perform various image synthesis tasks through gradient-based optimization. For a comprehensive discussion of these approaches, see Appendix A.1.

3 Method

3.1 Joint Energy-Based Model

Our approach builds upon the Joint Energy-Based Model (JEM) framework introduced by Grathwohl et al. (2019), which reinterprets the outputs of a standard discriminative classifier as an energy-based model (EBM) over the joint distribution of data x and labels y . Given a classifier network that produces logits $f_\theta(x) \in \mathbb{R}^K$ for K classes, JEM defines the joint energy function as:

$$E_\theta(x, y) = -f_\theta(x)[y] \quad (1)$$

where $f_\theta(x)[y]$ is the logit corresponding to class y . This energy function can be normalized to obtain a joint probability density:

$$p_\theta(x, y) = \frac{\exp(-E_\theta(x, y))}{Z(\theta)} = \frac{\exp(f_\theta(x)[y])}{Z(\theta)} \quad (2)$$

where $Z(\theta) = \sum_{y'} \int \exp(f_\theta(x')[y']) dx'$ is the partition function (an intractable global normalizing constant). By marginalizing out the label y , a marginal density over the input data x can be obtained:

$$p_\theta(x) = \sum_y p_\theta(x, y) = \frac{\sum_y \exp(f_\theta(x)[y])}{Z(\theta)} \quad (3)$$

Thus, a valid energy function for $p_\theta(x)$ is given by:

$$E_\theta(x) = -\log \sum_y \exp(f_\theta(x)[y]) \quad (4)$$

This energy is related to the marginal density by $p_\theta(x) = \frac{\exp(-E_\theta(x))}{Z(\theta)}$.

A JEM is trained by maximizing the joint log-likelihood $\log p_\theta(x, y)$ over labeled training datapoints (x, y) drawn from an empirical joint distribution $p_{\text{data}}(x, y)$. The joint log-likelihood is typically factorized as $\log p_\theta(y|x) + \log p_\theta(x)$. The conditional term $\log p_\theta(y|x)$ can be maximized by minimizing the standard cross-entropy classification loss. The marginal term $\log p_\theta(x)$ is optimized using the EBM gradient (LeCun et al., 2006):

$$\nabla_\theta \mathbb{E}_{x \sim p_{\text{data}}(x)} [\log p_\theta(x)] = \mathbb{E}_{x \sim p_{\text{data}}(x)} [-\nabla_\theta E_\theta(x)] - \mathbb{E}_{x \sim p_\theta(x)} [-\nabla_\theta E_\theta(x)] \quad (5)$$

where $p_{\text{data}}(x)$ is the empirical marginal distribution obtained by marginalizing y from $p_{\text{data}}(x, y)$. This gradient decreases the energy of real data samples while increasing the energy of model-generated samples. At equilibrium when $p_\theta(x) = p_{\text{data}}(x)$, these terms balance and the gradient becomes zero.

To approximate the expectation $\mathbb{E}_{x \sim p_\theta(x)}[\cdot]$, samples are drawn from $p_\theta(x)$ using Stochastic Gradient Langevin Dynamics (SGLD) (Welling and Teh, 2011). SGLD generates samples x starting from an initial distribution $p_0(x)$ (e.g., uniform noise) and iteratively applies the update rule:

$$x_{t+1} = x_t - \frac{\alpha}{2} \nabla_x E_\theta(x_t) + \xi_t, \quad \text{where } \xi_t \sim \mathcal{N}(0, \alpha) \quad (6)$$

Here, α is the step size, and $\nabla_x E_\theta(x_t)$ is the gradient with respect to the marginal energy function.

3.2 Learning JEM with adversarial training

The JEM framework successfully integrates generative modeling into classifiers, but its reliance on SGLD and EBM gradient (Eq. 5) causes significant training instabilities (Grathwohl et al., 2019; Duvenaud et al., 2021) and results in poor sample quality. We address these limitations by replacing the SGLD-based JEM with an adversarial training (AT) approach inspired by AT-EBMs (Yin et al., 2022).

Specifically, we replace the standard EBM gradient (Eq. 5) with a stabilized formulation:

$$\begin{aligned} & \mathbb{E}_{x \sim p_{\text{data}}(x)} [-\nabla_\theta E_\theta(x)] - \mathbb{E}_{x \sim p_\theta(x)} [-\nabla_\theta E_\theta(x)] \\ \implies & \mathbb{E}_{x \sim p_{\text{data}}(x)} [-\alpha(x) \nabla_\theta E_\theta(x)] - \mathbb{E}_{x \sim p_\theta(x)} [-\beta(x) \nabla_\theta E_\theta(x)] \end{aligned} \quad (7)$$

where $\alpha(x) = 1 - \sigma(-E_\theta(x))$ and $\beta(x) = \sigma(-E_\theta(x))$ are data-dependent scaling factors, and σ denotes the logistic sigmoid function. This formulation preserves the structural form of Eq. 5 while introducing adaptive scaling factors that modulate gradient contributions according to the model’s current energy assignments. According to Yin et al. (2022), these scaling factors stabilize training by providing automatic gradient regularization: as $-E_\theta(x)$ increases for p_{data} samples, the corresponding scaling factor $\alpha(x) = 1 - \sigma(-E_\theta(x))$ approaches zero, thereby attenuating the gradient contribution from such samples and preventing numerical overflow; conversely, when $-E_\theta(x)$ becomes very negative for contrastive samples, $\beta(x) = \sigma(-E_\theta(x))$ approaches zero, preventing numerical underflow. In contrast, the standard EBM gradient (Eq. 5) is unconstrained and permits $-E_\theta(x)$ to achieve arbitrarily large or small magnitudes, resulting in numerical instability during optimization. This gradient formulation stabilizes training at the cost of limiting the EBM to modeling the support of p_{data} rather than learning the full density. We provide a formal characterization of the learned distribution in Section A.15, where we show that the optimal solution under our joint objective learns $f_\theta^*(x)[y] = \log p_{\text{data}}(y|x)$ on the support with constant marginal energy $E_\theta^*(x) = 0$.

In addition to the above gradient reformulation, the sampling required to estimate $\mathbb{E}_{x \sim p_\theta(x)}[\cdot]$ is performed using the PGD attack (Madry et al., 2017) instead of SGLD. Specifically, the contrastive samples x from the model distribution are generated by initializing from an auxiliary out-of-distribution dataset p_{ood} (e.g., the 80 million tiny images dataset for CIFAR-10 training) and performing T iterations of gradient ascent on the negative energy function $-E_\theta(x)$:

$$x_{t+1} = x_t + \eta \frac{\nabla_x(-E_\theta(x_t))}{\|\nabla_x(-E_\theta(x_t))\|_2}, \quad t = 0, 1, \dots, T-1 \quad (8)$$

where $E_\theta(x)$ is the marginal energy function defined in Eq. 4, η is the step size, and T is the total number of PGD steps. Using the update direction suggested by Eq. 7 is equivalent to minimizing the Binary Cross-Entropy (BCE) loss:

$$\mathcal{L}_{\text{BCE}}(\theta) = -\mathbb{E}_{x \sim p_{\text{data}}(x)}[\log(\sigma(-E_\theta(x)))] - \mathbb{E}_{x \sim p_\theta(x)}[\log(1 - \sigma(-E_\theta(x)))] \quad (9)$$

(i.e., $\nabla_\theta \mathcal{L}_{\text{BCE}}$ equals the right-hand side of Eq. 7). Minimizing this \mathcal{L}_{BCE} implicitly trains the energy function $E_\theta(x)$ to assign low energy to data samples from $p_{\text{data}}(x)$ and high energy to the contrastive samples computed using the PGD attack.

We find this AT-based approach effectively addresses JEM’s training stability issues and produces high quality samples.

3.3 Classifier robustness and implicit regularization

Classifier robustness. While our AT-based approach improves the generative capabilities of JEM, the original JEM’s discriminative component still exhibits weak adversarial robustness compared to dedicated adversarially trained classifiers. To address this limitation, we complement our generative improvements by incorporating adversarial training for the discriminative term $p_\theta(y|x)$.

For each input sample x with label y , we find an adversarial example x_{adv} within an ϵ -ball $B(x, \epsilon)$ around x that maximizes the classification loss:

$$x_{\text{adv}} = \arg \max_{x' \in B(x, \epsilon)} \mathcal{L}_{\text{CE}}(\theta; x', y) \quad (10)$$

where $\mathcal{L}_{\text{CE}}(\theta; x', y)$ is the standard cross-entropy loss and $B(x, \epsilon)$ is an L_p -norm ball. Similar to our generative component, we approximate this optimization using the PGD attack (Madry et al., 2017), generating adversarial examples through iterative gradient steps within the constraint set. The classification term is then defined as:

$$\mathcal{L}_{\text{AT-CE}}(\theta) = \mathbb{E}_{(x, y) \sim p_{\text{data}}(x, y)} [-\log p_\theta(y|x_{\text{adv}})] \quad (11)$$

Implicit regularization. Incorporating AT for the classifier not only ensures robust accuracy but also yields a synergistic benefit for the generative component. Specifically, it functionally replaces the R_1 gradient penalty (Mescheder et al., 2018), an explicit regularization required by the original AT-EBMs framework (Yin et al., 2022) that can constrain model expressiveness. Our theoretical analysis demonstrates that AT inherently provides implicit regularization that encompasses R_1 -style penalties through its first-order penalty on gradient norms (see Section A.2). We empirically validate

this through quantitative measurements showing that adversarial training maintains bounded R_1 gradients throughout training, while standard training exhibits gradient explosion (Section A.13). While AT and explicit R_1 penalty operate at different scales and through different objectives, this quantitative evidence confirms that the local smoothness induced by AT effectively substitutes for explicit R_1 penalties, enabling stable EBM training without additional regularization.

3.4 Dual AT for joint modeling

Our complete model integrates adversarial training principles for both the generative and discriminative components, resulting in the combined objective:

$$\mathcal{L}(\theta) = \mathcal{L}_{\text{AT-CE}}(\theta) + \mathcal{L}_{\text{BCE}}(\theta) \quad (12)$$

where $\mathcal{L}_{\text{AT-CE}}(\theta)$ is the robust classification loss from Eq. 11, and $\mathcal{L}_{\text{BCE}}(\theta)$ is the AT-based generative loss from Eq. 9. This DAT approach simultaneously enhances the model’s discriminative robustness and generative capabilities, addressing the key limitations of the original JEM framework; full algorithmic details are provided in Appendix A.3.

Our approach shares conceptual similarities with RATIO (Augustin et al., 2020), which also combines adversarially robust classification with adversarial perturbations applied to out-of-distribution data:

$$\mathcal{L}_{\text{RATIO}}(\theta) = \mathcal{L}_{\text{AT-CE}}(\theta) + \lambda \mathbb{E}_{x \sim p_{\text{ood}}(x)} \left[\max_{x' \in B(x, \epsilon_o)} \mathcal{L}_{\text{CE}}(\theta; x', \mathbf{1}/K) \right] \quad (13)$$

where $\mathbf{1}$ is the vector of all ones and K is the number of classes. Despite this structural similarity, the approaches differ fundamentally in their objectives. RATIO’s secondary term attacks OOD samples to maximize classifier confidence, then penalizes this confidence via cross-entropy against a uniform distribution, explicitly targeting robust OOD detection. In contrast, our $\mathcal{L}_{\text{BCE}}(\theta)$ leverages AT-based energy function learning (Yin et al., 2022), using PGD to generate contrastive samples from OOD data and employing BCE loss to shape the energy landscape. While RATIO focuses primarily on reducing confidence in OOD regions, our approach prioritizes learning a stable and effective energy function that enables high-quality generative modeling alongside robust classification.

3.5 Two-stage training

Neural network architectures typically incorporate normalization layers to stabilize and speed up training: ResNet (He et al., 2016) uses batch normalization (BN) (Ioffe and Szegedy, 2015), while modern architectures like ConvNeXt (Liu et al., 2022) and Vision Transformers (Dosovitskiy et al., 2021; Vaswani et al., 2017) utilize layer normalization (Ba et al., 2016). Training energy-based joint models presents unique challenges with normalization layers. In particular, batch normalization has been identified as problematic for EBM training (Grathwohl et al., 2019; Yin et al., 2022; Zhao et al., 2020). Consistent with these findings, we observe that enabling BN during joint training destabilizes the optimization of the generative modeling term \mathcal{L}_{BCE} , leading to oscillating losses and failure to converge.

To address these challenges while maintaining the benefits of normalization during discriminative training, we propose a two-stage training strategy that generalizes effectively across diverse architectures:

- **Stage 1: Discriminative training.** We first train the network with its original normalization configuration, optimizing only the robust classification objective $\mathcal{L}_{\text{AT-CE}}$ (Eq. 11). This stage is equivalent to standard adversarial training and leverages normalization layers to achieve faster convergence and strong robust classification performance. Notably, this stage can be skipped when pretrained robust classifiers are available, making our approach immediately applicable to existing robust models.
- **Stage 2: Joint training.** After robust discriminative training, we modify the normalization behavior when necessary and continue training with the complete objective $\mathcal{L}(\theta) = \mathcal{L}_{\text{AT-CE}}(\theta) + \mathcal{L}_{\text{BCE}}(\theta)$ (Eq. 12). For architectures with batch normalization (ResNet, WRN), we disable BN by setting BN modules to eval mode, which freezes the BN statistics computed during Stage 1. For architectures with layer normalization (ConvNeXt), we maintain the normalization as-is.

This strategy not only addresses the incompatibility between batch normalization and EBM training, but also enables leveraging pretrained robust classifiers to dramatically reduce training costs (see Section A.14 for detailed computational analysis). As demonstrated in Section 4.3, Stage 2 improves the generative modeling performance of pretrained robust classifiers while incurring minimal impact on the robust accuracy established in Stage 1 (see Section A.12 for training dynamics). Importantly, the two-stage training strategy works effectively for both ResNet and ConvNeXt models, making it suitable for architectures with better scaling properties such as Vision Transformers (Dosovitskiy et al., 2021; Singh et al., 2023; Peebles and Xie, 2023a).

3.6 Data augmentation

Strong data augmentations are necessary for achieving robust classification (Rebuffi et al., 2021; Goyal et al., 2020) but can distort the data distribution in ways detrimental to generative modeling. We therefore follow Yang et al. (2023) and apply separate augmentation strategies to the discriminative and generative components. While Yang et al. (2023) concludes that augmentations like random cropping with padding should be excluded from generative training to avoid artifacts like black borders, we find this is not a limitation in our framework. Notably, even with random cropping and padding applied, our generated samples do not inherit these artifacts, allowing us to improve robustness without degrading sample quality (see Section A.4.2). We therefore apply strong augmentations to the discriminative term $\mathcal{L}_{\text{AT-CE}}$ and mild augmentations to the generative term \mathcal{L}_{BCE} .

4 Experiments

4.1 Training setup

Datasets and architectures. We evaluate our approach on CIFAR-10 (Krizhevsky et al., 2009), CIFAR-100 (Krizhevsky et al., 2009), and ImageNet (Deng et al., 2009). For CIFAR-10/100 experiments, we use WRN-34-10 (Zagoruyko and Komodakis, 2016) following the official RATIO implementation. For ImageNet experiments, we employ ResNet-50 (He et al., 2016), WRN-50-4 (Zagoruyko and Komodakis, 2016), and ConvNeXt-Large with ConvStem (Singh et al., 2023).

Two-stage training. Since Stage 1 training is equivalent to standard adversarial training, we use pretrained standard AT checkpoints when available: a standard AT checkpoint from the RATIO codebase (Augustin et al., 2020) for CIFAR-10, pretrained ImageNet ResNet-50 and WRN-50-4 models from Salman et al. (2020), and pretrained ConvNeXt-Large with ConvStem from Singh et al. (2023) (originally trained for $\ell_\infty = 4/255$ robustness), while training our own CIFAR-100 model following Augustin et al. (2020). For Stage 2 training, we initialize from the Stage 1 model and continue joint training. For ResNet and WRN architectures, we set the BN modules to eval mode (which disables BN while preserving the BN statistics computed during Stage 1). Complete training hyperparameters can be found in Section A.4.1.

Data augmentation. We employ separate data augmentation strategies for Stage 2 training: strong augmentations for $\mathcal{L}_{\text{AT-CE}}$ and basic transformations for \mathcal{L}_{BCE} to preserve the data distribution. Detailed specifications can be found in Section A.4.2.

Out-of-distribution data. Same as RATIO, we use the 80 million tiny images (Torralba et al., 2008) as the OOD dataset (p_{ood}) for CIFAR-10/100 experiments. For ImageNet, as there are no established OOD datasets, we follow OpenImage-O (Wang et al., 2022b) and construct an OOD dataset from Open Images training set (Krasin et al., 2016). We randomly sample 350K images, restricting our selection to those whose labels do not overlap with any ImageNet classes, yielding 300K samples for training and 50K for FID evaluation.

4.2 Evaluation metrics

We measure both classification and generative modeling performance. For classification, we report clean accuracy and robust accuracy against L_2 attacks ($\epsilon = 0.5$ for CIFAR-10/100 and $\epsilon = 3.0$ for ImageNet) computed using AutoAttack (Croce and Hein, 2020). For generative modeling, we evaluate sample diversity and visual fidelity using Fréchet Inception Distance (FID) (Heusel et al.,

2017) and Inception Score (IS) (Salimans et al., 2016). We focus on conditional generation; details of the generation setup are provided in Section A.6.

To measure the quality of counterfactuals, we generate sets of counterfactual examples by applying targeted attacks to training samples across a range of perturbation limits. For each target class, we compute the class-wise FID score between the set of counterfactuals targeted at that class and the set of training samples from the same class. Note that counterfactuals are generated by applying PGD attacks to in-distribution training samples, whereas generative modeling samples are created by applying PGD attacks to OOD inputs.

4.3 Results

4.3.1 Classification and generative modeling

We evaluate the proposed approach on CIFAR-10, CIFAR-100, and ImageNet 256×256 (Tables 1 and 2). Our results demonstrate three distinctive capabilities: (1) the first EBM-based hybrid to scale to high-resolution complex datasets, (2) unique combination of state-of-the-art generative quality with adversarial robustness, and (3) competitive performance as a standalone generative model.

First EBM-based hybrid to scale to high-resolution datasets with adversarial robustness. Prior EBM-based hybrid approaches (JEM, SADA-JEM) are not explicitly optimized for adversarial robustness. On CIFAR-10, these methods achieve significantly lower robust accuracy than standard AT: JEM achieves 40.5% and SADA-JEM achieves 31.93%, compared to 75.73% for standard AT (Table 1). Our approach addresses this limitation, achieving 75.75% robust accuracy—comparable to standard AT—while improving generative quality over prior EBM hybrids: FID 9.12 versus 38.4 (JEM) and 9.41 (SADA-JEM). Beyond robustness, prior EBM-based hybrids could not scale beyond low resolution or achieve competitive generative performance on ImageNet-level datasets. Our approach is the first to overcome this limitation: on ImageNet 256×256 , our ConvNeXt-Large model achieves FID 3.29 (Table 2) with classification performance comparable to standard AT (Section A.17), demonstrating that EBM-based hybrid models can scale reliably to complex, high-resolution datasets while achieving strong classification performance.

Combining generative quality with adversarial robustness. While other scalable hybrids exist, they do not simultaneously achieve both strong adversarial robustness and state-of-the-art generative quality. The diffusion-based EGC achieves 13.56% robust accuracy on ImageNet compared to our 56.40%, while also achieving worse FID (6.05 vs. 3.29) (Table 2). Similarly, RATIO targets robustness but not generation quality (FID 21.96 vs. our 9.12 on CIFAR-10). Qualitatively, Figures 5, 6, and 7 show that our method produces visually superior samples with fewer artifacts compared to RATIO and standard AT. This unique combination of generative quality and robustness enables critical applications such as robust counterfactual explanations (Section 4.3.2), where our model produces substantially higher-quality counterfactuals than both non-robust and robustness-only methods.

Competitive as a standalone generative model. When evaluated purely on generation quality, our approach achieves performance competitive with state-of-the-art specialized generative models. On ImageNet 256×256 , DAT with ConvNeXt-L achieves FID 3.29, matching the state-of-the-art autoregressive model VAR-d16 (FID 3.30) while using fewer parameters (198M vs. 310M) and outperforming leading diffusion models including ADM-G (FID 4.59, 608M parameters) and LDM-4-G (FID 3.60, 400M parameters) (Table 2). The model also achieves relatively strong IS performance (310.2), likely due to PGD-based sampling explicitly optimizing for classifier confidence. Figure 8 shows representative samples demonstrating the visual quality achieved by our approach. Beyond quality, our approach achieves significantly higher throughput than diffusion models: $\sim 29\times$ faster than ADM-G and $\sim 5\times$ faster than LDM-4-G (Table 17).

Trading off generative and discriminative performance. Our experiments reveal that the number of PGD training steps (T in Eq. 8) controls the balance between discriminative and generative performance. On CIFAR-10, increasing T from 40 to 50 improves FID from 9.12 to 7.57 at the cost of standard and robust accuracy. A similar trend is observed on CIFAR-100 and ImageNet, where increasing T consistently improves generation quality while reducing classification performance.

Effect of model capacity and architecture. Our experiments on ImageNet demonstrate the benefits of increased model capacity and modern architectures. Scaling from ResNet-50 (26M parameters) to

WRN-50-4 (223M parameters) yields consistent improvements across both discriminative and generative metrics. Beyond capacity, using state-of-the-art architectures also provides substantial benefits: ConvNeXt-L (198M parameters) substantially outperforms WRN-50-4 (223M parameters) in both accuracy and generation quality despite having fewer parameters, demonstrating the importance of architectural design alongside model scale.

Table 1: Classification and generative modeling results on CIFAR-10 and CIFAR-100.

Method	Acc% \uparrow	Robust Acc% \uparrow	IS \uparrow	FID \downarrow
<i>CIFAR-10 hybrid models</i>				
Residual Flow (Chen et al., 2019)	70.3	—	3.6	46.4
Glow (Kingma and Dhariwal, 2018)	67.6	—	3.92	48.9
IGEBM (Du and Mordatch, 2019)	49.1	—	8.3	37.9
JEM (Grathwohl et al., 2019)	92.9	40.5	8.76	38.4
VERA (Grathwohl et al., 2021)	93.2	—	8.11	30.5
JEM++ (Yang and Ji, 2021)	94.1	—	8.11	38.0
JEAT (Zhu et al., 2021)	85.16	—	8.80	38.24
Robust-JEM (Korst and Asadulaev, 2022)	—	—	8.71	41.17
SADA-JEM (Yang et al., 2023)	95.5	31.93	8.77	9.41
WEAT (Mirza et al., 2024)	83.36	—	8.97	30.74
EGC (Guo et al., 2023)	95.9	—	9.43	3.30
Joint-Diffusion (Deja et al., 2023)	96.4	—	—	6.4
RATIO (Augustin et al., 2020)	92.23	76.25	9.61	21.96
Standard AT (Augustin et al., 2020)	92.43	75.73	9.58	28.41
DAT ($T = 40$)	91.92	75.75	9.92	9.12
DAT ($T = 50$)	90.72	74.65	9.86	7.57
<i>CIFAR-10 conditional generative models</i>				
SNGAN (Miyato et al., 2018)	—	—	8.59	25.5
BigGAN (Brock et al., 2018)	—	—	9.22	14.73
StyleGAN2 (Karras et al., 2020a)	—	—	9.53	6.96
StyleGAN2 ADA (Karras et al., 2020b)	—	—	10.24	3.49
EDM (Karras et al., 2022)	—	—	—	1.79
<i>CIFAR-100 hybrid models</i>				
Joint-Diffusion (Deja et al., 2023)	77.6	—	—	16.8
SADA-JEM (Yang et al., 2023)	75.0	—	11.63	14.4
EGC (Guo et al., 2023)	77.9	—	11.50	4.88
RATIO (Augustin et al., 2020)	71.58	47.74	9.28	24.17
Standard AT (Augustin et al., 2020)	72.16	47.78	9.54	23.59
DAT ($T = 45$)	65.76	45.94	10.99	10.73
DAT ($T = 50$)	60.12	42.55	11.12	9.53

4.3.2 Counterfactual generation, OOD detection, and calibration

Counterfactual generation. Figure 1 compares counterfactual quality across different models while accounting for classifier confidence. Our approach consistently generates counterfactuals with lower FIDs than baseline methods when achieving similar target class confidence. For instance, when the RATIO baseline reaches approximately 0.89 confidence in the target class (at $\epsilon = 8$), its corresponding FID is 43.18. Our DAT model achieves a similar confidence level at $\epsilon = 4$ with a significantly better FID of 25.53. This demonstrates that, for a comparable level of certainty that the counterfactual represents the target class, our generated samples are substantially more faithful to the true visual characteristics of that class, indicating more plausible counterfactuals. Therefore, our model’s improved generative capabil-

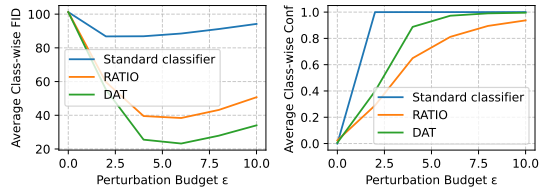


Figure 1: Counterfactual FIDs and classifier confidences under different perturbations.

Table 2: Classification and conditional generative modeling results on ImageNet 256×256.

Method	Acc% \uparrow	Robust Acc% \uparrow	FID \downarrow	IS \uparrow	Params	Steps
<i>Hybrid models</i>						
EGC (Guo et al., 2023)	78.90	13.56	6.05	231.3	543M (U-Net)	1000
Standard AT (Salman et al., 2020)	64.91	39.96	15.12	286.2	26M (ResNet-50)	13
DAT ($T = 15$)	61.31	39.96	6.87	322.65	26M (ResNet-50)	14
DAT ($T = 30$)	55.96	37.14	5.28	319.3	26M (ResNet-50)	14
Standard AT (Salman et al., 2020)	71.25	45.86	37.33	260.2	223M (WRN-50-4)	12
DAT ($T = 30$)	64.45	45.84	6.23	341.0	223M (WRN-50-4)	17
DAT ($T = 65$)	58.78	40.74	4.94	358.0	223M (WRN-50-4)	19
Standard AT (Singh et al., 2023)	78.25	33.38	44.46	27.32	198M (ConvNext-L-CvSt)	0
DAT ($T = 110$)	75.78	56.40	3.29	310.2	198M (ConvNext-L-CvSt)	36
<i>Conditional generative models</i>						
BigGAN-deep (Brock et al., 2018)	–	–	6.95	203.6	340M (ResNet)	1
ADM-G (Dhariwal and Nichol, 2021)	–	–	4.59	186.7	608M (U-Net)	250
LDM-4-G (Rombach et al., 2022)	–	–	3.60	247.7	400M (U-Net)	250
DiT-XL/2-G (Peebles and Xie, 2023b)	–	–	2.27	278.2	675M (Transformers)	250
VAR-d16 (Tian et al., 2024)	–	–	3.30	274.4	310M (Transformers)	10
VAR-d30-re (Tian et al., 2024)	–	–	1.73	350.2	2.0B (Transformers)	10

ity directly translates to higher-quality counterfactual explanations, enhancing model explainability. We provide visualizations of counterfactuals in Section A.9.

OOD detection. Our approach generally underperforms RATIO on OOD detection. Ablation studies show this gap persists even when using identical aggressive augmentation for both the generative and discriminative components, indicating it stems from fundamental objective differences rather than the use of milder augmentation for the generative term: RATIO explicitly optimizes for OOD detection while our generative loss prioritizes learning accurate energy functions for generation. The complete details can be found in Section A.7

Calibration. Our model’s calibration performance is dataset-dependent, with detailed results provided in Section A.8. While the model is well-calibrated on CIFAR-10, outperforming the standard AT and RATIO baselines, it exhibits higher overconfidence on CIFAR-100 and ImageNet. The results suggest that prioritizing generative quality may come at the cost of calibration.

4.3.3 Additional analyses

In Section A.5 we conduct additional analyses including component ablation of DAT, OOD dataset effects, and loss weighting mechanisms. Component ablation reveals that both the generative loss and decoupled augmentation contribute to the improved generative quality compared to a standard AT baseline (Section A.5.1). OOD dataset analysis demonstrates notable data efficiency of our approach, suggesting strong performance is achievable even with limited auxiliary OOD data (Section A.5.2). Loss weighting analysis confirms that re-weighting the two loss terms provides an alternative mechanism for controlling the generative-discriminative trade-off beyond varying PGD steps (Section A.5.3). Beyond adversarial robustness, we evaluate robustness to common corruptions (Hendrycks and Dietterich, 2019), demonstrating that our approach maintains strong corruption robustness comparable to standard AT (Section A.16). Regarding computational efficiency, our two-stage training incurs modest overhead relative to standard adversarial training, while achieving significantly faster inference throughput than diffusion models (Section A.14). Our empirical analyses reveal an inherent trade-off between generative and discriminative performance, which can be controlled through mechanisms such as PGD step count and loss weighting; we provide a detailed discussion of this trade-off and its underlying mechanism in Section A.18. To demonstrate the stability and reproducibility of our approach, we report mean and standard deviation across five independent runs for CIFAR-10, CIFAR-100, and ImageNet in Section A.11.

5 Conclusion

We presented Dual Adversarial Training (DAT), demonstrating that hybrid models can achieve state-of-the-art performance without compromise. Our approach advances hybrid modeling in three ways: (1) we present the first EBM-based hybrid to scale to high-resolution complex datasets, achieving FID 3.29 and competitive robust accuracy on ImageNet 256×256 ; (2) we uniquely combine state-of-the-art generative quality with adversarial robustness, enabling critical applications such as robust counterfactual explanations; and (3) as a standalone generative model, our approach matches the generative quality of state-of-the-art autoregressive methods and surpasses leading diffusion models while offering unique versatility for diverse synthesis tasks.

Future work could advance this approach in several directions: improving training efficiency with persistent markov chains, scaling the framework to higher-capacity architectures such as ConvNeXt-XLarge and Vision Transformers; improving secondary tasks like out-of-distribution detection by developing hybrid objectives that combine our generative loss with RATIO's; and applying the model to broader image synthesis tasks such as those demonstrated by Santurkar et al. (2019).

References

- Andrew Y Ng and Michael I Jordan. On discriminative vs. generative classifiers: A comparison of logistic regression and naive Bayes. In *Advances in Neural Information Processing Systems*, volume 14, 2001.
- Tony Jebara. *Machine Learning: Discriminative and Generative*. The Springer International Series in Engineering and Computer Science. Springer, New York, NY, 2004.
- Julia A Lasserre, Christopher M Bishop, and Thomas P Minka. Principled hybrids of generative and discriminative models. In *2006 IEEE Computer Society Conference on Computer Vision and Pattern Recognition (CVPR'06)*, volume 1, pages 87–94. IEEE, 2006.
- Jianwen Xie, Yang Lu, Song-Chun Zhu, and Yingnian Wu. A theory of generative convnet. In *International conference on machine learning*, pages 2635–2644. PMLR, 2016.
- Will Grathwohl, Kuan-Chieh Wang, Jörn-Henrik Jacobsen, David Duvenaud, Mohammad Norouzi, and Kevin Swersky. Your classifier is secretly an energy based model and you should treat it like one. *arXiv preprint arXiv:1912.03263*, 2019.
- Justin Lazarow, Long Jin, and Zhuowen Tu. Introspective neural networks for generative modeling. In *Proceedings of the IEEE International Conference on Computer Vision*, pages 2774–2783, 2017.
- Long Jin, Justin Lazarow, and Zhuowen Tu. Introspective classification with convolutional nets. *Advances in Neural Information Processing Systems*, 30, 2017.
- Yilun Du and Igor Mordatch. Implicit generation and modeling with energy based models. *Advances in neural information processing systems*, 32, 2019.
- Ricky TQ Chen, Jens Behrmann, David K Duvenaud, and Jörn-Henrik Jacobsen. Residual flows for invertible generative modeling. *Advances in Neural Information Processing Systems*, 32, 2019.
- Qiushan Guo, Chuofan Ma, Yi Jiang, Zehuan Yuan, Yizhou Yu, and Ping Luo. Egc: Image generation and classification via a diffusion energy-based model. In *Proceedings of the IEEE/CVF International Conference on Computer Vision*, pages 22952–22962, 2023.
- Kamil Deja, Tomasz Trzcinski, and Jakub M Tomczak. Learning data representations with joint diffusion models. In *Joint European Conference on Machine Learning and Knowledge Discovery in Databases*, pages 543–559. Springer, 2023.
- David Duvenaud, Jacob Kelly, Kevin Swersky, Milad Hashemi, Mohammad Norouzi, and Will Grathwohl. No mcmc for me: Amortized samplers for fast and stable training of energy-based models. In *International Conference on Learning Representations (ICLR)*, 2021.
- Yang Zhao, Jianwen Xie, and Ping Li. Learning energy-based generative models via coarse-to-fine expanding and sampling. In *International Conference on Learning Representations*, 2020.
- Ruiqi Gao, Yang Lu, Junpei Zhou, Song-Chun Zhu, and Ying Nian Wu. Learning generative convnets via multi-grid modeling and sampling. In *Proceedings of the IEEE Conference on Computer Vision and Pattern Recognition*, pages 9155–9164, 2018.
- Erik Nijkamp, Mitch Hill, Song-Chun Zhu, and Ying Nian Wu. Learning non-convergent non-persistent short-run mcmc toward energy-based model. *Advances in Neural Information Processing Systems*, 32, 2019.
- Aleksander Madry, Aleksandar Makelov, Ludwig Schmidt, Dimitris Tsipras, and Adrian Vladu. Towards deep learning models resistant to adversarial attacks. *arXiv preprint arXiv:1706.06083*, 2017.
- Xuwang Yin, Shiyang Li, and Gustavo K Rohde. Learning energy-based models with adversarial training. In *European Conference on Computer Vision*, pages 209–226. Springer, 2022.
- Yilun Du, Shuang Li, and Igor Mordatch. Compositional visual generation with energy based models. In *Advances in Neural Information Processing Systems*, volume 33, pages 6637–6647, 2020.

- Shibani Santurkar, Andrew Ilyas, Dimitris Tsipras, Logan Engstrom, Brandon Tran, and Aleksander Madry. Image synthesis with a single (robust) classifier. *Advances in Neural Information Processing Systems*, 32, 2019.
- Diederik P Kingma, Danilo Jimenez Rezende, Shakir Mohamed, and Max Welling. Semi-supervised learning with deep generative models. In *Advances in Neural Information Processing Systems*, volume 27, 2014.
- Xiulong Yang, Qing Su, and Shihao Ji. Towards bridging the performance gaps of joint energy-based models. In *Proceedings of the IEEE/CVF Conference on Computer Vision and Pattern Recognition*, pages 15732–15741, 2023.
- Kwonjoon Lee, Weijian Xu, Fan Fan, and Zhuowen Tu. Wasserstein introspective neural networks. In *Proceedings of the IEEE conference on computer vision and pattern recognition*, pages 3702–3711, 2018.
- Max Welling and Yee W Teh. Bayesian learning via stochastic gradient langevin dynamics. In *Proceedings of the 28th international conference on machine learning (ICML-11)*, pages 681–688. Citeseer, 2011.
- Yao Zhu, Jiacheng Ma, Jiacheng Sun, Zewei Chen, Rongxin Jiang, Yaowu Chen, and Zhenguo Li. Towards understanding the generative capability of adversarially robust classifiers. In *Proceedings of the IEEE/CVF International Conference on Computer Vision*, pages 7728–7737, 2021.
- Yifei Wang, Yisen Wang, Jiansheng Yang, and Zhouchen Lin. A unified contrastive energy-based model for understanding the generative ability of adversarial training. In *International Conference on Learning Representations*, 2022a.
- Mujtaba Hussain Mirza, Maria Rosaria Briglia, Senad Beadini, and Iacopo Masi. Shedding more light on robust classifiers under the lens of energy-based models. In *European Conference on Computer Vision*, pages 449–466. Springer, 2024.
- Maximilian Augustin, Alexander Meinke, and Matthias Hein. Adversarial robustness on in-and out-distribution improves explainability. In *European Conference on Computer Vision*, pages 228–245. Springer, 2020.
- Rostislav Korst and Arip Asadulaev. Adversarial training improves joint energy-based generative modelling. *arXiv preprint arXiv:2207.08950*, 2022.
- Yann LeCun, Sumit Chopra, Raia Hadsell, Marc’Aurelio Ranzato, and Fu-Jie Huang. A tutorial on energy-based learning. In *Predicting Structured Data*, pages 1–59. MIT Press, 2006.
- Lars Mescheder, Andreas Geiger, and Sebastian Nowozin. Which training methods for gans do actually converge? In *International conference on machine learning*, pages 3481–3490. PMLR, 2018.
- Kaiming He, Xiangyu Zhang, Shaoqing Ren, and Jian Sun. Deep residual learning for image recognition. In *Proceedings of the IEEE Conference on Computer Vision and Pattern Recognition*, pages 770–778, 2016.
- Sergey Ioffe and Christian Szegedy. Batch normalization: Accelerating deep network training by reducing internal covariate shift. In *International conference on machine learning*, pages 448–456. pmlr, 2015.
- Zhuang Liu, Hanzi Mao, Chao-Yuan Wu, Christoph Feichtenhofer, Trevor Darrell, and Saining Xie. A convnet for the 2020s. In *Proceedings of the IEEE/CVF Conference on Computer Vision and Pattern Recognition*, pages 11976–11986, 2022.
- Alexey Dosovitskiy, Lucas Beyer, Alexander Kolesnikov, Dirk Weissenborn, Xiaohua Zhai, Thomas Unterthiner, Mostafa Dehghani, Matthias Minderer, Georg Heigold, Sylvain Gelly, Jakob Uszkoreit, and Neil Houlsby. An image is worth 16x16 words: Transformers for image recognition at scale. In *International Conference on Learning Representations*, 2021.

- Ashish Vaswani, Noam Shazeer, Niki Parmar, Jakob Uszkoreit, Llion Jones, Aidan N Gomez, Łukasz Kaiser, and Illia Polosukhin. Attention is all you need. In *Advances in Neural Information Processing Systems*, volume 30, pages 6000–6010, 2017.
- Jimmy Lei Ba, Jamie Ryan Kiros, and Geoffrey E Hinton. Layer normalization. *arXiv preprint arXiv:1607.06450*, 2016.
- Naman D Singh, Francesco Croce, and Matthias Hein. Revisiting adversarial training for imagenet: Architectures, training and generalization across threat models. In *Advances in Neural Information Processing Systems*, volume 36, pages 54424–54443, 2023.
- William Peebles and Saining Xie. Scalable diffusion models with transformers. In *Proceedings of the IEEE/CVF International Conference on Computer Vision*, pages 4195–4205, 2023a.
- Sylvestre-Alvise Rebuffi, Sven Gowal, Dan A Calian, Florian Stimberg, Olivia Wiles, and Timothy Mann. Fixing data augmentation to improve adversarial robustness. *arXiv preprint arXiv:2103.01946*, 2021.
- Sven Gowal, Chongli Qin, Jonathan Uesato, Timothy Mann, and Pushmeet Kohli. Uncovering the limits of adversarial training against norm-bounded adversarial examples. *arXiv preprint arXiv:2010.03593*, 2020.
- Alex Krizhevsky, Geoffrey Hinton, et al. Learning multiple layers of features from tiny images. 2009.
- Jia Deng, Wei Dong, Richard Socher, Li-Jia Li, Kai Li, and Li Fei-Fei. Imagenet: A large-scale hierarchical image database. In *2009 IEEE Conference on Computer Vision and Pattern Recognition*, pages 248–255. IEEE, 2009.
- Sergey Zagoruyko and Nikos Komodakis. Wide residual networks. In *Proceedings of the British Machine Vision Conference*, 2016.
- Hadi Salman, Andrew Ilyas, Logan Engstrom, Ashish Kapoor, and Aleksander Madry. Do adversarially robust imagenet models transfer better? *Advances in Neural Information Processing Systems*, 33:3533–3545, 2020.
- Antonio Torralba, Rob Fergus, and William T Freeman. 80 million tiny images: A large data set for nonparametric object and scene recognition. *IEEE transactions on pattern analysis and machine intelligence*, 30(11):1958–1970, 2008.
- Haoqi Wang, Zhizhong Li, Litong Feng, and Wayne Zhang. Vim: Out-of-distribution with virtual-logit matching. In *Proceedings of the IEEE/CVF conference on computer vision and pattern recognition*, pages 4921–4930, 2022b.
- Ivan Krasin, Tom Duerig, Neil Alldrin, Andreas Veit, Sami Abu-El-Haija, Serge Belongie, David Cai, Zheyun Feng, Vittorio Ferrari, Victor Gomes, Abhinav Gupta, Dhyanesh Narayanan, Chen Sun, and Gal Chechik. Openimages: A public dataset for large-scale multi-label and multi-class image classification. 2016. Dataset available from <https://storage.googleapis.com/openimages/web/index.html>.
- Francesco Croce and Matthias Hein. Reliable evaluation of adversarial robustness with an ensemble of diverse parameter-free attacks. In *International conference on machine learning*, pages 2206–2216. PMLR, 2020.
- Martin Heusel, Hubert Ramsauer, Thomas Unterthiner, Bernhard Nessler, and Sepp Hochreiter. Gans trained by a two time-scale update rule converge to a local nash equilibrium. In *Advances in Neural Information Processing Systems*, 2017.
- Tim Salimans, Ian Goodfellow, Wojciech Zaremba, Vicki Cheung, Alec Radford, and Xi Chen. Improved techniques for training gans. In *Advances in Neural Information Processing Systems*, 2016.
- Durk P Kingma and Prafulla Dhariwal. Glow: Generative flow with invertible 1x1 convolutions. *Advances in neural information processing systems*, 31, 2018.

- Will Grathwohl, Jacob Kelly, Milad Hashemi, Mohammad Norouzi, Kevin Swersky, and David Duvenaud. No mcmc for me: Amortized sampling for fast and stable training of energy-based models. In *International Conference on Learning Representations*, 2021.
- Xiulong Yang and Shihao Ji. Jem++: Improved techniques for training jem. In *Proceedings of the IEEE/CVF International Conference on Computer Vision*, pages 6494–6503, 2021.
- Takeru Miyato, Toshiki Kataoka, Masanori Koyama, and Yuichi Yoshida. Spectral normalization for generative adversarial networks. *arXiv preprint arXiv:1802.05957*, 2018.
- Andrew Brock, Jeff Donahue, and Karen Simonyan. Large scale gan training for high fidelity natural image synthesis. *arXiv preprint arXiv:1809.11096*, 2018.
- Tero Karras, Samuli Laine, Miika Aittala, Janne Hellsten, Jaakko Lehtinen, and Timo Aila. Analyzing and improving the image quality of stylegan. In *Proceedings of the IEEE/CVF conference on computer vision and pattern recognition*, pages 8110–8119, 2020a.
- Tero Karras, Miika Aittala, Janne Hellsten, Samuli Laine, Jaakko Lehtinen, and Timo Aila. Training generative adversarial networks with limited data. *Advances in neural information processing systems*, 33:12104–12114, 2020b.
- Tero Karras, Miika Aittala, Timo Aila, and Samuli Laine. Elucidating the design space of diffusion-based generative models. In *Advances in Neural Information Processing Systems*, volume 35, pages 26565–26577, 2022.
- Prafulla Dhariwal and Alexander Nichol. Diffusion models beat gans on image synthesis. *Advances in neural information processing systems*, 34:8780–8794, 2021.
- Robin Rombach, Andreas Blattmann, Dominik Lorenz, Patrick Esser, and Björn Ommer. High-resolution image synthesis with latent diffusion models. In *Proceedings of the IEEE/CVF conference on computer vision and pattern recognition*, pages 10684–10695, 2022.
- William Peebles and Saining Xie. Scalable diffusion models with transformers. In *Proceedings of the IEEE/CVF International Conference on Computer Vision*, pages 4195–4205, 2023b.
- Keyu Tian, Yi Jiang, Zehuan Yuan, Bingyue Peng, and Liwei Wang. Visual autoregressive modeling: Scalable image generation via next-scale prediction. *arXiv preprint arXiv:2404.02905*, 2024.
- Dan Hendrycks and Thomas Dietterich. Benchmarking neural network robustness to common corruptions and perturbations. *International Conference on Learning Representations*, 2019.
- AMD. Amd instinct mi300x accelerator. <https://www.amd.com/en/products/accelerators/instinct/mi300/mi300x.html>, 2024. Accessed: 2024.
- Lambda Labs. Gpu benchmarks for deep learning. <https://lambda.ai/gpu-benchmarks>, 2024. Accessed: 2024.

A Supplementary Material

A.1 Extended discussion on related work

Connections between adversarial robustness and energy-based models Zhu et al. (2021) reinterpret adversarially trained classifiers as joint energy-based models, showing that adversarial training implicitly flattens the energy landscape around real data by reducing the energy of nearby high-energy adversarial examples. They identify $E_\theta(x, y)$ as the key energy term for conditional generation and propose JEAT, which employs energy-based adversarial perturbations and SGLD sampling for likelihood estimation and generation. Mirza et al. (2024) extend this analysis by decomposing the cross-entropy loss as $\mathcal{L}_{\text{CE}}(x, y; \theta) = E_\theta(x, y) - E_\theta(x)$, revealing that untargeted attacks increase the joint energy $E_\theta(x^*, y)$ (reducing classifier confidence of class y) while decreasing the marginal energy $E_\theta(x^*)$. They show that robust overfitting corresponds to divergence between $E_\theta(x)$ and $E_\theta(x^*)$, and that state-of-the-art robust models achieve better generalization by smoothing the marginal energy landscape around natural data. Wang et al. (2022a) proposed a unified Contrastive Energy-based Model (CEM) framework that interprets adversarial training as biased maximum likelihood estimation of an energy-based model $p_\theta(x, y) = \exp(f_\theta(x, y))/Z(\theta)$. Unlike JEM (Grathwohl et al., 2019) which samples negative examples from random noise via Langevin dynamics, CEM shows that PGD-generated adversarial perturbations from real data serve as implicit negative samples, providing more stable training without requiring random noise or OOD data. The framework unifies supervised (P-CEM) and unsupervised (NP-CEM) scenarios, revealing connections between adversarial training, contrastive learning, and energy-based modeling, and enables improved sampling algorithms that achieve state-of-the-art generative performance. While these works provide valuable insights into the energy-based interpretation of adversarial training, training methods that rely on SGLD-based sampling (e.g., JEAT) inherit the instabilities of standard JEM (Grathwohl et al., 2019). In contrast, our work addresses these stability issues by employing PGD-based contrastive sampling and replacing the unstable EBM loss with a standard BCE loss.

Learning EBMs with adversarial training Yin et al. (2022) explored an alternative approach to learning EBMs by leveraging the mechanism of Adversarial Training (AT). They established a connection between the objective of binary AT (discriminating real data from adversarially perturbed out-of-distribution data) and the SGLD-based maximum likelihood training commonly used for EBMs. Specifically, they showed that the binary classifier learned via AT implicitly defines an energy function that models the support of the data distribution, assigning low energy to in-distribution regions and high energy to out-of-distribution (OOD) regions. The PGD attack used in AT to generate adversarial samples from OOD data was interpreted as a non-convergent sampler that produces contrastive data, analogous to MCMC sampling in EBM training. Although the resulting energy function can only capture the support rather than recover the exact density, their model achieves competitive image generation performance compared to explicit EBMs. Notably, this AT-based EBM learning approach is more stable than traditional MCMC-based EBM training and demonstrated strong performance in worst-case out-of-distribution detection, similar to methods like RATIO (Augustin et al., 2020). However, AT-EBM focuses on unconditional generative modeling and employs an explicit R_1 gradient penalty to stabilize training, which can constrain model expressiveness. Our work incorporates AT-based EBM learning into the JEM framework to perform conditional generative modeling with implicit R_1 regularization from adversarial training, using ancestral sampling from the conditional distribution $p(x|y)$ rather than the marginal distribution $p(x)$.

Improving joint energy-based models Building on the original JEM framework (Grathwohl et al., 2019), several works have explored techniques to improve training stability and performance. Yang and Ji (2021) (JEM++) introduced multiple training improvements: (1) Proximal SGLD that constrains samples within an L_p -norm ball of previous samples via gradient clamping for improved stability; (2) YOPO-inspired acceleration (PYLD) that reduces redundant backpropagation by exploiting the coupling between samples and first-layer weights; (3) Informative initialization from a class-conditional Gaussian mixture distribution estimated from training data, which accelerates SGLD convergence, improves stability, and enables batch normalization. Korst and Asadulaev (2022) (Robust-JEM) further enhanced JEM++ by incorporating adversarial training into the discriminative component, empirically observing improved training stability. At inference time, they propose a "combined inference" approach where initial samples from PGD adversarial attacks are refined using SGLD, improving generative performance. However, both JEM++ and Robust-JEM fundamentally still rely on SGLD for sampling and MLE-based objectives for the generative component, inheriting

SGLD’s intrinsic instability issues. While these works introduced valuable techniques for improving SGLD stability, they did not fundamentally resolve the instability of SGLD-based training and both remain limited to CIFAR-scale (32×32) datasets. Our approach departs fundamentally from this line of work by: (1) providing mathematical analysis and empirical evidence showing that adversarial training offers implicit R_1 regularization (Section A.2); (2) replacing the MLE-based objective with BCE-based gradients; (3) using deterministic PGD-based sampling instead of stochastic Langevin dynamics; and (4) introducing a two-stage training strategy to address the incompatibility between batch normalization and EBM training. This enables scaling to high-resolution ImageNet synthesis (256×256) with state-of-the-art generative quality.

In- and out-distribution adversarial robustness Addressing the multifaceted challenge of creating models that are simultaneously accurate, robust, and reliable on out-of-distribution (OOD) data, Augustin et al. (2020) proposed **RATIO** (Robustness via Adversarial Training on In- and Out-distribution). Their approach combines standard adversarial training (AT) on the in-distribution data, aimed at improving robustness against adversarial examples, with a form of AT on OOD data, which enforces low and uniform confidence predictions within a neighborhood around OOD samples. The combined objective trains the model to maintain correct, robust classifications for in-distribution data while actively discouraging high-confidence predictions for OOD inputs, even under adversarial manipulation. Augustin et al. (2020) demonstrated that **RATIO** achieves state-of-the-art L_2 robustness on datasets like CIFAR-10, often with less degradation in clean accuracy compared to standard AT alone. Furthermore, they showed that **RATIO** yields reliable OOD detection performance, particularly in worst-case scenarios where OOD samples are adversarially perturbed to maximize confidence. Their work also highlighted that the L_2 robustness fostered by **RATIO** enables the generation of meaningful visual counterfactual explanations directly in pixel space, where optimizing confidence towards a target class results in the emergence of corresponding class-specific visual features.

Robust classifiers for image synthesis and manipulation Santurkar et al. (2019) demonstrated that adversarially robust classifiers can serve as powerful primitives for diverse image synthesis tasks. The core insight of their work is that the process of adversarial training—which optimizes the worst-case loss over an ℓ_2 perturbation set rather than expected loss—compels a model to learn more perceptually aligned and human-interpretable feature representations by preventing reliance on imperceptible artifacts. Based on this insight, Santurkar et al. (2019) showed that simple gradient ascent on class scores from such robust classifiers enables a unified framework for image generation, inpainting, image-to-image translation, super-resolution, and interactive manipulation—tasks typically requiring specialized GAN architectures or complex generative models.

A.2 Adversarial training as implicit R_1 regularization

We provide mathematical analysis demonstrating that adversarial training inherently provides implicit R_1 regularization, eliminating the need for explicit gradient penalties. For classification tasks, consider a vector-valued function $f : \mathbb{R}^d \rightarrow \mathbb{R}^K$ producing logits for K classes.

R_1 regularization directly penalizes large gradients of the true class logit:

$$\mathcal{L}_{R_1} = \mathbb{E}_{(x,y) \sim p_{\text{data}}} \left[\|\nabla_x f_y(x)\|_2^2 \right] \quad (14)$$

In practice, adversarial training uses cross-entropy loss to enforce consistent predictions:

$$\mathcal{L}_{\text{AT}} = \mathbb{E}_{(x,y) \sim p_{\text{data}}} \left[\max_{\|\delta\|_2 \leq \epsilon} L(f(x + \delta), y) \right] \quad (15)$$

To understand how adversarial training provides implicit gradient regularization, we analyze the first-order behavior of this cross-entropy adversarial objective.

First-order expansion of the adversarial objective. Let $z = f(x) \in \mathbb{R}^K$, $p = \text{softmax}(z)$, and $J_f(x) \in \mathbb{R}^{K \times d}$ be the input-Jacobian of the logits. For cross-entropy loss $L(z, y) = -\log p_y$, a first-order Taylor expansion gives:

$$L(f(x + \delta), y) = L(f(x), y) + \nabla_x L(f(x), y)^T \delta + O(\|\delta\|_2^2) \quad (16)$$

$$\max_{\|\delta\|_2 \leq \epsilon} L(f(x + \delta), y) \approx L(f(x), y) + \epsilon \|\nabla_x L(f(x), y)\|_2 \quad (17)$$

This approximation is valid for sufficiently small ϵ relative to the local curvature of L , such that higher-order terms remain negligible over the L_2 constraint ball $\{\delta : \|\delta\|_2 \leq \epsilon\}$.

This shows that adversarial training implicitly adds a penalty term proportional to $\|\nabla_x L\|_2$ (the first power of the gradient norm). To understand what this gradient represents, we apply the chain rule:

$$\nabla_x L = J_f(x)^T \nabla_z L = J_f(x)^T (p - e_y) \quad (18)$$

where e_y is the one-hot label vector. Let $g_k(x) := \nabla_x f_k(x) \in \mathbb{R}^d$ denote the per-class input gradients (the rows of J_f). Then we can write:

$$\nabla_x L = \sum_{k=1}^K (p_k - \delta_{ky}) g_k = -(1 - p_y) g_y + \sum_{k \neq y} p_k g_k \quad (19)$$

This decomposition reveals that the cross-entropy gradient is a weighted combination of per-class gradients, where the true class gradient g_y appears with negative weight $(1 - p_y)$ and competitor gradients g_k appear with positive weights p_k .

Expansion into R_1 -style components. To understand how this relates to standard R_1 regularization, we can expand the squared gradient norm by substituting the final expression for $\nabla_x L$. Although the actual adversarial penalty is proportional to $\|\nabla_x L\|_2$, examining $\|\nabla_x L\|_2^2$ provides useful analytical insight:

$$\|\nabla_x L\|_2^2 = \left\| -(1 - p_y) g_y + \sum_{k \neq y} p_k g_k \right\|_2^2 \quad (20)$$

Expanding this expression:

$$\begin{aligned} \|\nabla_x L\|_2^2 = & \underbrace{(1 - p_y)^2 \|g_y\|_2^2}_{\text{down-weighted true-class } R_1} + \underbrace{\sum_{k \neq y} p_k^2 \|g_k\|_2^2}_{\text{competitor } R_1 \text{ terms}} \\ & - 2(1 - p_y) \underbrace{\sum_{k \neq y} p_k \langle g_y, g_k \rangle}_{\text{true vs competitor alignment}} + 2 \underbrace{\sum_{\substack{i < j \\ i, j \neq y}} p_i p_j \langle g_i, g_j \rangle}_{\text{competitor-competitor alignment}} \end{aligned} \quad (21)$$

This expansion decomposes the adversarial penalty into interpretable components:

1. **True-class R_1 regularization:** $(1 - p_y)^2 \|g_y\|_2^2$, which is the standard R_1 penalty on the true class, down-weighted by confidence
2. **Competitor R_1 terms:** $\sum_{k \neq y} p_k^2 \|g_k\|_2^2$, providing R_1 -style regularization on competing classes weighted by their predicted probabilities
3. **Gradient alignment terms:** Cross-class inner products $\langle g_i, g_j \rangle$ that discourage competitor–competitor alignment (favoring orthogonality), while encouraging the true-class gradient to align with the competitor average

This decomposition reveals that the adversarial training objective contains the core R_1 regularization term $(1 - p_y)^2 \|g_y\|_2^2$ on the true class, confirming that adversarial training inherently penalizes large gradients as R_1 does. Beyond this, adversarial training introduces richer regularization through competitor R_1 terms weighted by predicted probabilities and gradient alignment constraints between classes. Notably, the $(1 - p_y)^2$ factor means the true-class R_1 penalty diminishes on high-confidence predictions and strengthens on uncertain ones—an adaptive behavior absent in uniform R_1 penalties.

Empirical validation. We validate this theoretical analysis by tracking R_1 gradient norms during ImageNet training (Section A.13). As predicted by the analysis above, adversarial training on the discriminative loss maintains bounded and stable R_1 gradients throughout training, while standard training exhibits gradient explosion—with R_1 values spiking to much higher levels. While our analysis relies on first-order approximations that may not strictly hold for the ϵ values used in practice, and the actual adversarial penalty is proportional to $\|\nabla_x L\|_2$ rather than its square, the empirical observations are consistent with the theoretical predictions. This confirms that implicit regularization from adversarial training suffices to maintain bounded R_1 gradients, thereby enabling stable energy-based model training.

A.3 DAT training algorithm

The complete training procedure for our combined objective (Eq. 12) is detailed in Algorithm 1. We note that to train the generative component \mathcal{L}_{BCE} , we sample from $p_\theta(x)$ to estimate $\mathbb{E}_{x \sim p_\theta(x)}[-\nabla_\theta E_\theta(x)]$ in Eq. 5. In the context of JEM, there are broadly two strategies for drawing samples from $p_\theta(x)$ (Grathwohl et al., 2019):

1. Direct sampling from the marginal distribution using gradient-based MCMC (e.g., SGLD or PGD) on the marginal energy $E_\theta(x) = -\log \sum_y \exp(f_\theta(x)[y])$, as implied by Eq. 8.
2. Ancestral sampling, which first draws a label $y \sim p_{\text{data}}(y)$, then samples $x \sim p_\theta(x|y)$ by running gradient-based MCMC on the joint energy $E_\theta(x, y) = -f_\theta(x)[y]$.

Although both approaches yield unbiased estimates, we find ancestral sampling to be practically superior for training stability, possibly because it leverages the classifier’s existing strong class representations to provide better mode coverage and mixing properties, while direct sampling from the marginal distribution often diverges. We also find ancestral sampling (conditional generation) yields substantially better FID than directly sampling from marginal distribution (see Table 11).

Consequently, our implementation adopts ancestral sampling when generating contrastive samples (Algorithm 1). Specifically, we first sample a label $y' \sim p_{\text{data}}(y)$, then generate a contrastive sample x_T by performing T iterations of PGD on the negative joint energy function $-E_\theta(x, y')$, starting from an initial sample $x_0 \sim p_{\text{ood}}$. This class-conditional contrastive sample x_T is then used in the \mathcal{L}_{BCE} objective (Eq. 9), whose gradient (Eq. 7) provide an approximation to Eq. 5.

Algorithm 1 DAT training: Given network logits f_θ , in-distribution dataset p_{data} , auxiliary out-of-distribution dataset p_{ood} , classification AT bound ϵ , PGD iterations T , PGD step size η

```

1: while not converged do
2:   Sample  $(x, y) \sim p_{\text{data}}(x, y)$ , apply aggressive augmentation to  $x$ 
3:   Sample  $\hat{x} \sim p_{\text{data}}(x)$ ,  $x_0 \sim p_{\text{ood}}(x)$ , apply mild augmentation to  $\hat{x}$  and  $x_0$ 
4:   Solve  $x_{\text{adv}} = \arg \max_{x' \in B(x, \epsilon)} \mathcal{L}_{\text{CE}}(\theta; x', y)$  via PGD attack
5:    $\mathcal{L}_{\text{AT-CE}}(\theta) = -\log p_\theta(y|x_{\text{adv}})$  ▷ Robust classification loss
6:   Initialize  $x_t \leftarrow x_0$  for  $t = 0$ , sample  $y' \sim p_{\text{data}}(y)$ 
7:   for  $t \in \{1, \dots, T\}$  do ▷ Generate contrastive sample for EBM
8:      $g = \nabla_x (-E_\theta(x_{t-1}, y'))$  ▷ Gradient of negative energy
9:      $x_t \leftarrow x_{t-1} + \eta \cdot g / \|g\|_2$  ▷ Normalized gradient ascent step
10:  end for
11:   $\mathcal{L}_{\text{BCE}}(\theta) = -\log(\sigma(-E_\theta(\hat{x}))) - \log(1 - \sigma(-E_\theta(x_T)))$  ▷ Generative modeling loss
12:   $\mathcal{L}(\theta) = \mathcal{L}_{\text{AT-CE}}(\theta) + \mathcal{L}_{\text{BCE}}(\theta)$ 
13:  Compute parameter gradients  $\nabla_\theta \mathcal{L}(\theta)$  and update  $\theta$ 
14: end while

```

A.4 Model training

A.4.1 Training details

We implement the two-stage training approach as described in Section 3.5. Table 3 summarizes the key hyperparameters used for both stages across different datasets.

For Stage 1, we utilize a pretrained CIFAR-10 model from RATIO (Augustin et al., 2020) and pretrained ImageNet ResNet-50 and WRN-50-4 models from Salman et al. (2020), while training our own CIFAR-100 model following the RATIO methodology with the hyperparameters specified in Table 3. For ConvNeXt-Large experiments on ImageNet, we use the pretrained robust checkpoint from Singh et al. (2023). We select the EMA model with the best robust test accuracy as the final Stage 1 model.

For Stage 2, we initialize from the Stage 1 model and continue training. For ResNet and WRN architectures, we disable batch normalization by setting all BN modules to evaluation mode. During this stage, we optimize the complete objective function $\mathcal{L}(\theta) = \mathcal{L}_{\text{AT-CE}}(\theta) + \mathcal{L}_{\text{BCE}}(\theta)$ using fixed learning rates as specified in Table 3. For the discriminative component $\mathcal{L}_{\text{AT-CE}}(\theta)$, CIFAR and ImageNet ResNet/WRN models continue to use the same adversarial settings as stage 1, while ConvNeXt transitions from L_∞ to L_2 perturbations with adjusted PGD parameters (see Table 4). The generative component $\mathcal{L}_{\text{BCE}}(\theta)$ employs the parameters detailed in Table 5.

We select the Stage 2 checkpoint with the best FID score for the final evaluation reported in Section 4.3.

Table 3: Training hyperparameters for both stages. Epochs for stage 2 are estimated based on the number of in-distribution images seen by the discriminative component during training.

	CIFAR-10/100	ImageNet	ImageNet
Architecture	WRN-34-10	ResNet-50/WRN-50-4	ConvNeXt-L-CvSt
BatchNorm	Enabled (stage 1), Disabled (stage 2)	Enabled (stage 1), Disabled (stage 2)	N/A
LayerNorm	N/A	N/A	Enabled
Optimizer	SGD with Nesterov	SGD with Nesterov	AdamW
Weight decay	5×10^{-4}	1×10^{-4} (stage 1), 5×10^{-4} (stage 2)	0.05
Batch size	128	512	756 (stage 1), 512 (stage 2)
EMA	Enabled	Enabled	Enabled
LR (stage 1)	0.1 (cosine schedule)	0.1 (step decay at epochs 30, 60, 90)	0.001 (cosine decay with warm-up)
LR (stage 2)	0.001 (CIFAR-10), 0.009 (CIFAR-100)	0.001	0.0003
Epochs (stage 1)	300	90	100
Epochs (stage 2)	26 (CIFAR-10), 30 (CIFAR-100)	0.78 (ResNet-50), 0.39 (WRN-50-4)	1.09

Table 4: Adversarial training parameters for $\mathcal{L}_{\text{AT-CE}}$ (identical across stages for CIFAR and ImageNet ResNet/WRN).

	CIFAR-10/100	ImageNet (ResNet/WRN)	ImageNet (ConvNeXt-L-CvSt)
PGD steps	10	2	2
PGD step size	0.1	2.0	2/255 (L_∞ , stage 1), 2.0 (L_2 , stage 2)
Perturbation bound	L_2 , $\epsilon = 0.5$	L_2 , $\epsilon = 3.0$	$\epsilon = 4/255$ (L_∞ , stage 1), $\epsilon = 3.0$ (L_2 , stage 2)

Table 5: Adversarial training parameters for \mathcal{L}_{BCE} (stage 2 only).

	CIFAR-10/100	ImageNet (ResNet/WRN)	ImageNet (ConvNeXt-L-CvSt)
Max PGD steps (T)	40/45/50	15/30/65	110
PGD step size	0.1	2.0	3.0
L_2 perturbation bound	None (unconstrained)	None (unconstrained)	None (unconstrained)
OOD data source	80M Tiny Images (Torralba et al., 2008)	Open Images (Krasin et al., 2016)	Open Images (Krasin et al., 2016)

A.4.2 Data augmentation details

As described in Section 3.6, we implement separate data augmentation pipelines for the discriminative and generative components of our objective function. Table 6 summarizes these augmentation strategies for stage 2 training. For CIFAR-10/100 and ImageNet ResNet/WRN, the pretrained models we initialize from were trained with the same augmentations as stage 2 $\mathcal{L}_{\text{AT-CE}}$ (from Augustin et al. (2020) for CIFAR and Salman et al. (2020) for ImageNet). For ImageNet ConvNeXt-L-CvSt, the pretrained model from Singh et al. (2023) was trained with heavy augmentations (RandAugment + MixUp + CutMix + Random Erasing), which differ from the simpler stage 2 $\mathcal{L}_{\text{AT-CE}}$ strategy shown in Table 6. The effects of CIFAR-10 augmentations are illustrated in Figure 2.

Figure 3 illustrates CIFAR-10 training curves from stage 2 joint training with various augmentation strategies applied to \mathcal{L}_{BCE} (while consistently using AutoAugment with Cutout for $\mathcal{L}_{\text{AT-CE}}$). Interestingly, the choice of augmentation for the generative component influences discriminative performance as well, as evidenced by the decline in robust test accuracy when using no augmentation. The best FID performance is achieved by no augmentation and random cropping with padding, which minimally distort the underlying data distribution p_{data} . Overall we find random cropping with padding provides the optimal balance between discriminative and generative performances.

Table 6: Data augmentation strategies for discriminative and generative components.

Dataset	Component	Augmentation Strategy
CIFAR-10/100	$\mathcal{L}_{\text{AT-CE}}$	AutoAugment + Cutout + RandomHorizontalFlip()
	\mathcal{L}_{BCE}	RandomCrop(32, padding=4) + RandomHorizontalFlip()
ImageNet	$\mathcal{L}_{\text{AT-CE}}$	RandomResizedCrop(256) + RandomHorizontalFlip()
	\mathcal{L}_{BCE}	Resize(256) + CenterCrop(256) + RandomHorizontalFlip()



Figure 2: Samples produced by different augmentations on CIFAR-10.

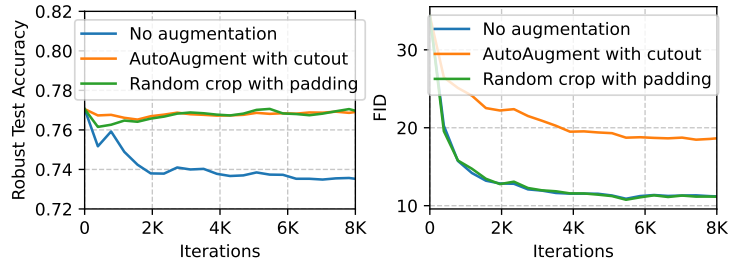


Figure 3: CIFAR-10 training curves under different data augmentations during stage 2 joint training.

A.5 Additional analyses

A.5.1 Individual contributions of generative loss and decoupled augmentation

To analyze the individual contribution of our primary contributions, we conduct an ablation study with the following variants on CIFAR-10:

- Standard AT: A baseline adversarially trained model without a generative component.
- DAT with uniform augmentation: Our DAT approach that applies the same aggressive augmentation for both the discriminative and generative objectives.
- DAT with decoupled augmentation: Our DAT approach that applies aggressive augmentation to the discriminative term and mild augmentation for the generative term.

The results in Table 7 demonstrate the impacts of the AT-based generative loss and decoupled augmentation. Introducing the generative loss component to the standard AT baseline significantly reduces the FID from 33.04 to 15.35, while robust accuracy remains comparable. The subsequent application of a decoupled augmentation strategy yields a further reduction in FID to 9.07.

Since both our approach and RATIO extend a standard AT baseline with an objective function that leverages out-of-distribution (OOD) data, it is instructive to compare their relative efficacy in enhancing generative fidelity. The RATIO objective, which is formulated for robust OOD detection, reduces the FID from 33.04 to 21.96. In contrast, our generative objective provides a much larger improvement, lowering the FID to 15.35. This comparison confirms that for the goal of enhancing sample quality, a dedicated generative loss is more effective than an auxiliary loss designed for OOD detection.

Table 7: Effect of generative loss and augmentation on CIFAR-10.

Method	Acc% \uparrow	Robust Acc% \uparrow	FID \downarrow
Standard AT	92.34	75.73	33.04
DAT (uniform aug)	92.68	75.93	15.35
DAT (decoupled aug)	91.86	75.66	9.07
RATIO (Augustin et al., 2020)	92.23	76.25	21.96

A.5.2 Effect of OOD dataset size

The out-of-distribution (OOD) dataset is a critical component of our training framework, as it provides the initialization samples for computing the negative samples in the generative loss term. The influence of this dataset can be understood through the EBM learning mechanism: a more diverse OOD dataset provides better coverage of the input space, allowing the PGD attack (acting as an MCMC sampler) to discover a broader range of spurious modes in the current energy landscape. These discovered modes are then eliminated as the main objective function is optimized. Given this crucial role, the diversity and scale of the OOD dataset are expected to influence model performance.

To examine the impact of OOD dataset size, we conducted an ablation study on ImageNet using our DAT ResNet-50 ($T = 15$) model with varying OOD dataset sizes: 1K, 10K, 100K, and the full 300K samples. As shown in Table 8, the FID score improves modestly from 6.96 with 1K samples to 6.64 with 300K samples. Classification accuracy remains stable across all dataset sizes, with similar robustness levels, indicating that the OOD dataset size primarily affects generation quality rather than discriminative performance.

These results demonstrate notable data efficiency, with only modest improvements when scaling from 1K to 300K OOD samples. A contributing factor to this efficiency is data augmentation: we employ RandomResizedCrop with scale=(0.08, 1.0) and aspect ratio=(0.75, 1.33), which can crop as little as 8% of the original image with varying aspect ratios, potentially amplifying the effective diversity of each sample. To investigate the contribution of augmentation, we include a baseline using 1K OOD samples without data augmentation. While augmentation provides clear benefits—improving FID from 8.00 to 6.96—even without augmentation, our approach substantially outperforms standard AT

in generation quality (FID 8.00 vs. 15.97). This indicates the data efficiency can be largely attributed to the AT-based EBM learning mechanism itself, where the PGD attack can effectively explore the energy landscape even from limited initialization points.

Table 8: Impact of OOD dataset size on ImageNet performance for DAT ResNet-50 ($T = 15$) with 224×224 generation.

Method	Acc% \uparrow	Robust Acc% \uparrow	FID \downarrow	IS \uparrow
Standard AT	62.83	34.44	15.97	274.90
DAT 1K w/o aug	57.50	33.80	8.00	320.64
DAT 1K	57.56	34.22	6.94	324.23
DAT 10K	57.82	34.70	6.84	320.78
DAT 100K	58.19	34.88	6.70	322.10
DAT 300K	57.88	34.84	6.64	339.55

A.5.3 Generative-discriminative trade-off via loss weighting

Our training objective, $\mathcal{L}(\theta) = \mathcal{L}_{\text{AT-CE}}(\theta) + \mathcal{L}_{\text{BCE}}(\theta)$, is a composite of a discriminative and a generative loss. This structure naturally raises the question of whether it is possible to trade off between these two capabilities by adjusting the relative weight of each component. To investigate this possibility, we perform experiments on CIFAR-10 with three distinct weighting configurations:

- Standard loss (equal weighting): $\mathcal{L}(\theta) = \mathcal{L}_{\text{AT-CE}}(\theta) + \mathcal{L}_{\text{BCE}}(\theta)$
- Emphasize generative modeling: $\mathcal{L}(\theta) = 0.6 \cdot \mathcal{L}_{\text{AT-CE}}(\theta) + 1.4 \cdot \mathcal{L}_{\text{BCE}}(\theta)$
- Emphasize classification: $\mathcal{L}(\theta) = 1.4 \cdot \mathcal{L}_{\text{AT-CE}}(\theta) + 0.6 \cdot \mathcal{L}_{\text{BCE}}(\theta)$

The results in Table 9 confirm that the balance between generative and discriminative performance can be tuned by adjusting the loss term weights. Emphasizing the generative component improves FID at the cost of slightly reduced classification performance, while emphasizing classification achieves the opposite effect. However, we note that our standard, unweighted loss corresponds to the natural factorization of the joint log-likelihood in the original JEM formulation: $\log p_\theta(x, y) = \log p_\theta(y|x) + \log p_\theta(x)$. This suggests that equal weighting is a principled default that performs well without requiring additional hyperparameter tuning.

Table 9: Trading off generative and discriminative performance by weighting loss terms.

Method	Acc% \uparrow	Robust Acc% \uparrow	FID \downarrow
Standard loss	91.88	75.73	9.09
Emphasize generative modeling	91.16	75.11	8.77
Emphasize classification	92.52	75.97	10.02

A.6 Generative performance evaluation

We evaluate generative performance using Fréchet Inception Distance (FID) and Inception Score (IS). FID is computed between 50K class-balanced generated samples and the full training set, while IS is computed on the same set of 50K generated samples.

Conditional generation. We generate an equal number of samples for each class. To generate samples for a given class y , we first sample an OOD data point x from the corresponding OOD data source, and then perform T steps of PGD attack according to:

$$x_{t+1} = x_t + \eta \frac{\nabla_x(-E_\theta(x_t, y))}{\|\nabla_x(-E_\theta(x_t, y))\|_2} \quad (22)$$

where T is the number of PGD steps and η is the corresponding step size (see Table 10).

Unconditional generation. For unconditional generation, we directly sample from the marginal distribution using PGD according to Eq. 8:

$$x_{t+1} = x_t + \eta \frac{\nabla_x(-E_\theta(x_t))}{\|\nabla_x(-E_\theta(x_t))\|_2}$$

The FID results for both conditional and unconditional generation across all datasets are presented in Table 11. We find conditional generation consistently outperforms unconditional generation across all the datasets.

Table 10: Sample generation parameters for FID and IS evaluation. The number of PGD steps for each model and dataset combination is determined through grid search.

Model	Dataset	PGD steps (T)	Step size	OOD data source
DAT	CIFAR-10 ($T = 40$)	33	0.2	80M Tiny Images
	CIFAR-10 ($T = 50$)	35	0.2	80M Tiny Images
	CIFAR-100 ($T = 45$)	32	0.2	80M Tiny Images
	CIFAR-100 ($T = 50$)	33	0.2	80M Tiny Images
	ImageNet (ResNet-50, $T = 15$)	14	8.0	Open Images
	ImageNet (ResNet-50, $T = 30$)	14	8.0	Open Images
	ImageNet (WRN-50-4, $T = 30$)	17	8.0	Open Images
	ImageNet (WRN-50-4, $T = 65$)	19	8.0	Open Images
	ImageNet (ConvNeXt-L-CvSt, $T = 110$)	36	8.0	Open Images
RATIO	CIFAR-10	31	0.2	80M Tiny Images
	CIFAR-100	14	0.2	80M Tiny Images
Standard AT	CIFAR-10	22	0.2	80M Tiny Images
	CIFAR-100	15	0.2	80M Tiny Images
	ImageNet (ResNet-50)	13	8.0	Open Images
	ImageNet (WRN-50-4)	11	8.0	Open Images
	ImageNet (ConvNeXt-L-CvSt)	0	8.0	Open Images

Table 11: FIDs of conditional and unconditional generation of our approach.

	CIFAR-10	CIFAR-100	ImageNet 224×224 (ResNet50, $T = 15$)
Conditional generation	9.07	10.70	6.64
Unconditional generation	20.57	13.56	18.67

A.7 Out-of-distribution detection

We evaluate both standard out-of-distribution (OOD) detection performance and worst-case OOD detection under adversarial perturbations using models trained with 224×224 generation. For standard OOD detection, we measure the AUROC scores between in-distribution test samples and unmodified OOD samples. For worst-case detection, we evaluate against adversarially perturbed OOD samples specifically optimized to maximize the OOD detection function output. Results are computed using all the in-distribution test samples and 1024 out-distribution samples. For generating adversarial OOD samples, we use L_2 -based perturbation limit of 1.0 for CIFAR-10/100 and 3.0 for ImageNet.

Energy-based detection. We use an energy-based function $s_\theta(x) = -E_\theta(x)$, which is proportional to $\log p_\theta(x)$ up to an additive constant. To find adversarial OOD inputs for this function, we employ a PGD attack to maximize the negative energy:

$$x_{adv} = \arg \max_{x' \in B(x, \epsilon_o)} -E_\theta(x') \quad (23)$$

where x is a clean OOD input and $B(x, \epsilon_o)$ represents an L_2 -ball of radius ϵ_o centered at x .

Maximum confidence detection. We employ a maximum confidence function $s_\theta(x) = \max_y p_\theta(y|x)$ that uses the confidence in the most likely class (also used by RATIO (Augustin et al., 2020)). For this detection function, following RATIO (Augustin et al., 2020), we compute adversarial OOD inputs by maximizing the cross-entropy loss against a uniform distribution:

$$x_{adv} = \arg \max_{x' \in B(x, \epsilon_o)} \mathcal{L}_{CE}(\theta; x', \mathbf{1}/K) \quad (24)$$

where $\mathbf{1}/K$ represents a uniform distribution over all K classes. Maximizing this loss encourages the model to produce a non-uniform (confident) prediction, thereby maximizing the detection function.

Table 12 presents a comparison of the above two OOD detection functions. The results reveal complementary strengths: the energy-based function ($-E_\theta(x)$) achieves near-perfect AUROC scores on uniform noise detection, while the maximum confidence function ($\max_y p_\theta(y|x)$) demonstrates superior performance on natural image OOD datasets. Based on these findings, we adopt the maximum confidence score for subsequent comparisons with other methods.

Table 13 presents comparative results across different baselines. Notably, our DAT model achieves OOD detection performance comparable to standard AT on natural image datasets (CIFAR-100, SVHN), despite incorporating an additional OOD dataset during training. This observation suggests that our generative training component primarily enhances generation quality rather than improving OOD detection capabilities beyond those provided by standard adversarial training.

Compared to RATIO, our model exhibits lower OOD detection performance across most datasets. To investigate whether this gap stems from our use of milder augmentations for the generative component, we trained an ablation model that applies RATIO’s aggressive augmentation strategy to both loss terms. The results show that this variant performs similarly to our standard DAT model and still underperforms RATIO. This finding indicates that the performance gap is not primarily caused by the augmentation strategy but rather by the fundamental differences in the training objectives: RATIO’s loss is explicitly optimized for OOD detection performance, while our generative loss prioritizes learning an accurate energy function for generation.

A potential avenue for addressing this limitation involves developing a hybrid objective that combines our generative loss with RATIO’s explicit OOD detection term. This approach is theoretically motivated by the complementary nature of these objectives: our generative component learns to model the energy landscape of in-distribution data while naturally assigning low probability to out-of-distribution regions, which aligns conceptually with RATIO’s strategy of enforcing low confidence predictions in neighborhoods around OOD samples. Such a hybrid formulation could potentially preserve the generative modeling benefits of our approach while recovering the superior OOD detection performance of RATIO. Future work could explore this direction by investigating appropriate weighting strategies between the generative and OOD detection terms to achieve optimal performance across both objectives.

Table 12: Comparison of OOD detection functions on CIFAR-10.

Method	CIFAR-100		SVHN		Uniform noise	
	Clean	Adversarial	Clean	Adversarial	Clean	Adversarial
DAT ($\max_y p_\theta(y x)$)	0.8709	0.6480	0.9609	0.8334	0.8922	0.8257
DAT ($-E_\theta(x)$)	0.8484	0.6647	0.8011	0.6046	0.9995	0.9983

Table 13: OOD detection performance (AUROC) with CIFAR-10 as ID dataset (JEM results are from Augustin et al. (2020)). All methods use the maximum confidence detection function $s_\theta(x) = \max_y p_\theta(y|x)$.

Method	CIFAR-100		SVHN		Uniform noise	
	Clean	Adversarial	Clean	Adversarial	Clean	Adversarial
JEM	0.8760	0.1920	0.8930	0.0730	0.1180	0.0250
Standard AT	0.8759	0.6364	0.9625	0.8306	0.8501	0.7902
DAT ($T = 40$, uniform aug)	0.8751	0.6261	0.9642	0.8303	0.9546	0.9254
DAT ($T = 40$)	0.8709	0.6480	0.9609	0.8334	0.8922	0.8257
RATIO	0.9157	0.7516	0.9843	0.9130	0.9999	0.9999

Table 14: OOD detection performance (AUROC) with CIFAR-100 as ID dataset.

Method	CIFAR-10		SVHN		Uniform noise	
	Clean	Adversarial	Clean	Adversarial	Clean	Adversarial
Standard AT	0.7430	0.4093	0.8700	0.4863	0.7858	0.5048
RATIO	0.7320	0.3795	0.8439	0.4356	0.7769	0.5881
DAT ($T = 45$)	0.7027	0.5145	0.8271	0.5823	0.4024	0.2283

Table 15: OOD detection performance (AUROC) with ImageNet as ID dataset.

Method	CIFAR-10		SVHN		Uniform noise	
	Clean	Adversarial	Clean	Adversarial	Clean	Adversarial
Standard AT (ResNet-50)	0.7235	0.5304	0.9239	0.8089	0.8678	0.8377
DAT (ResNet-50, $T = 15$)	0.6599	0.4870	0.8813	0.7754	0.6899	0.6268

A.8 Calibration

We assess model calibration using reliability diagrams on models trained with 224×224 generation. Figures 4, 5, and 6 show calibration diagrams for CIFAR-10, CIFAR-100, and ImageNet respectively.

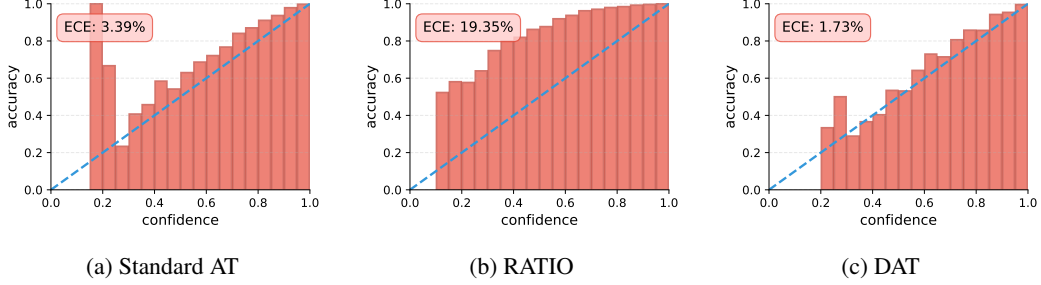


Figure 4: Calibration diagrams on CIFAR-10 (without temperature scaling).

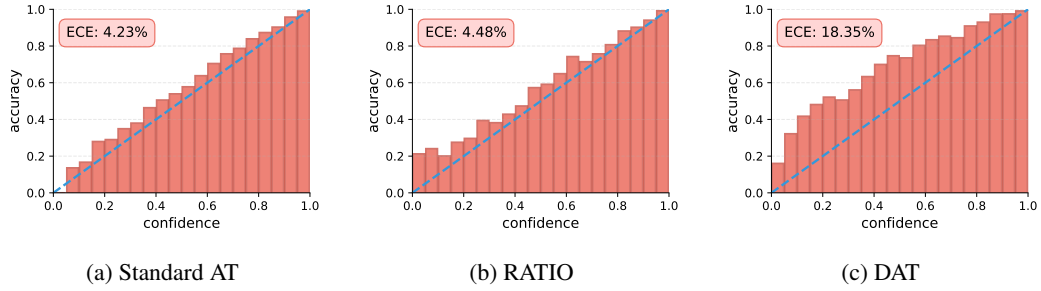


Figure 5: Calibration diagrams on CIFAR-100 (without temperature scaling).

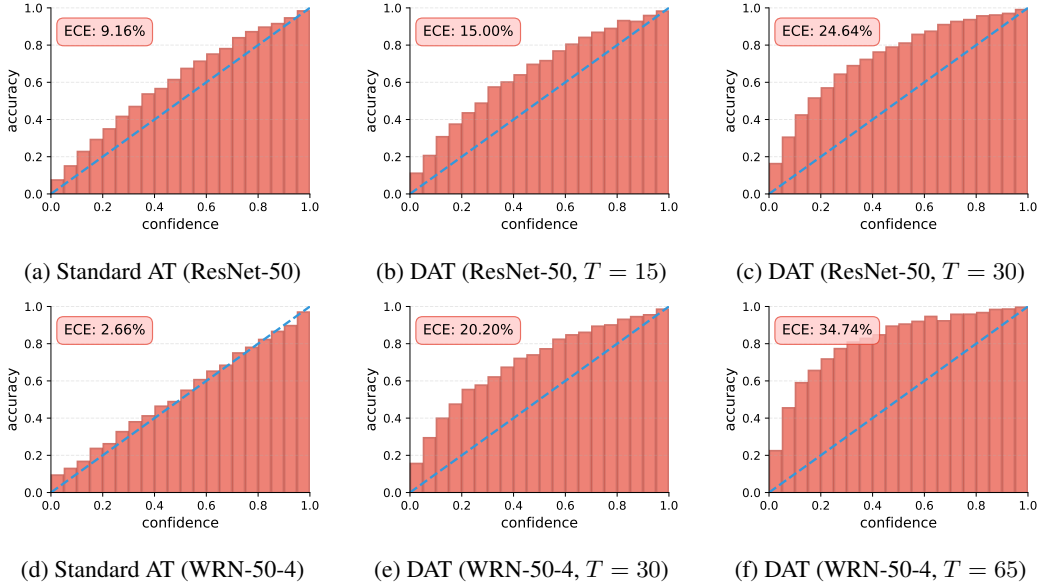


Figure 6: Calibration diagrams on ImageNet (without temperature scaling).

A.9 Counterfactual generation

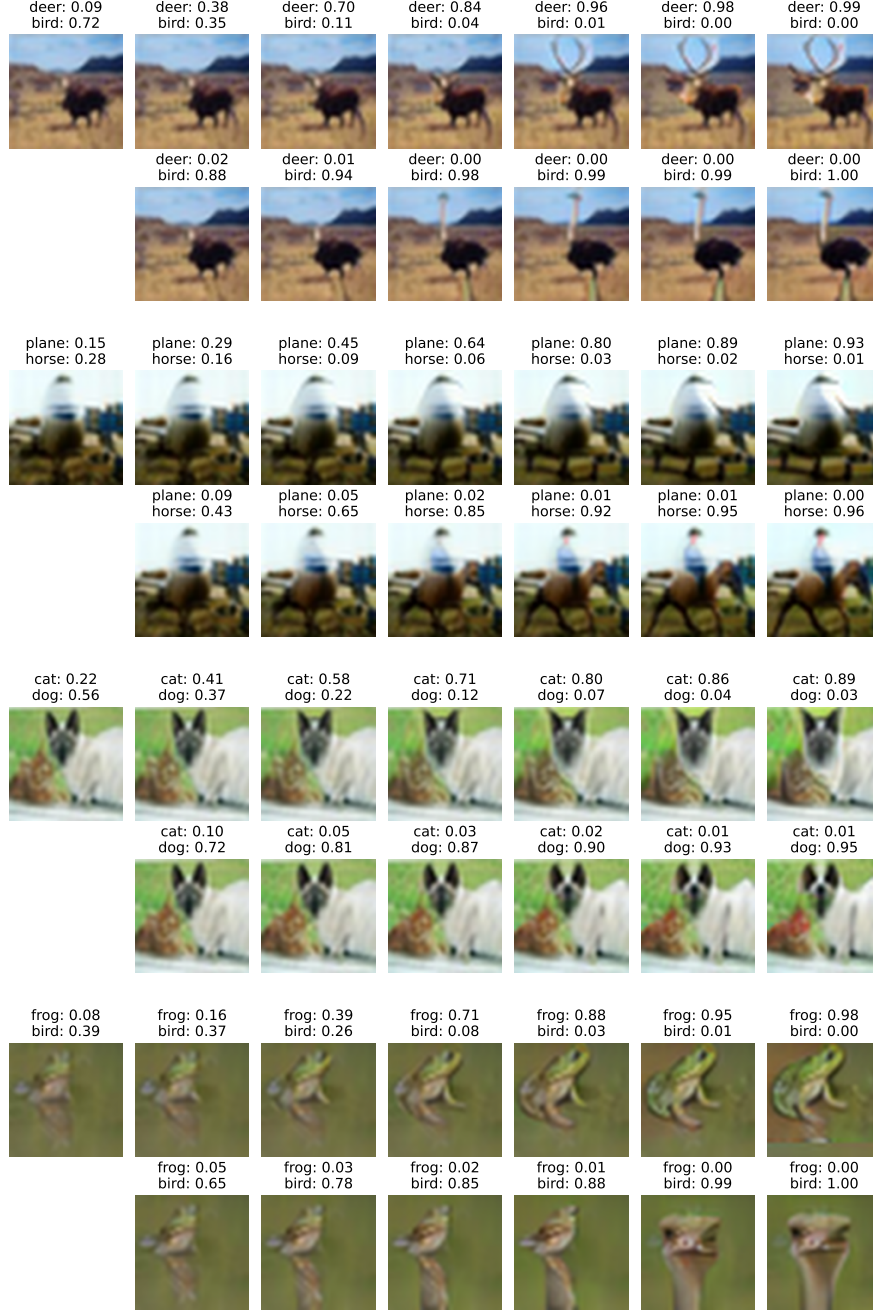


Figure 7: CIFAR-10 counterfactual examples with perturbation limits of 0.5, 1.0, 1.5, 2.0, 2.5, 3.0. These figures display counterfactuals and corresponding classifier confidences for both the correct class (top row) and a target wrong class (bottom row). As the perturbation budget increases from left to right, the generated counterfactuals progressively resemble samples from the target class distribution while the target class confidence correspondingly increases, demonstrating that our model effectively captures the distributions of different classes and can generate meaningful class-to-class transformations.

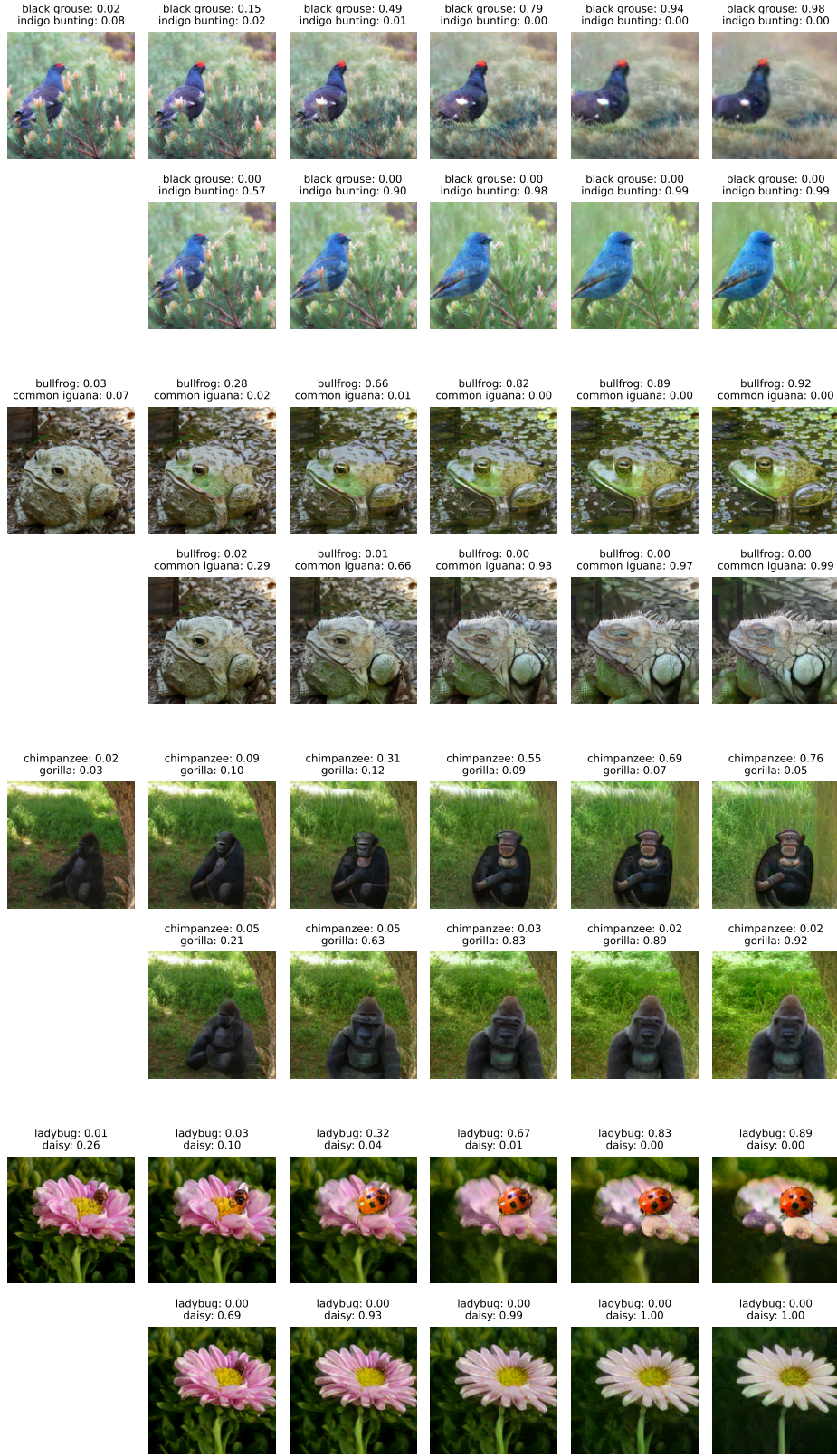


Figure 8: ImageNet counterfactual examples with perturbations limits of 10., 20., 30., 40., 50.

A.10 Generation results

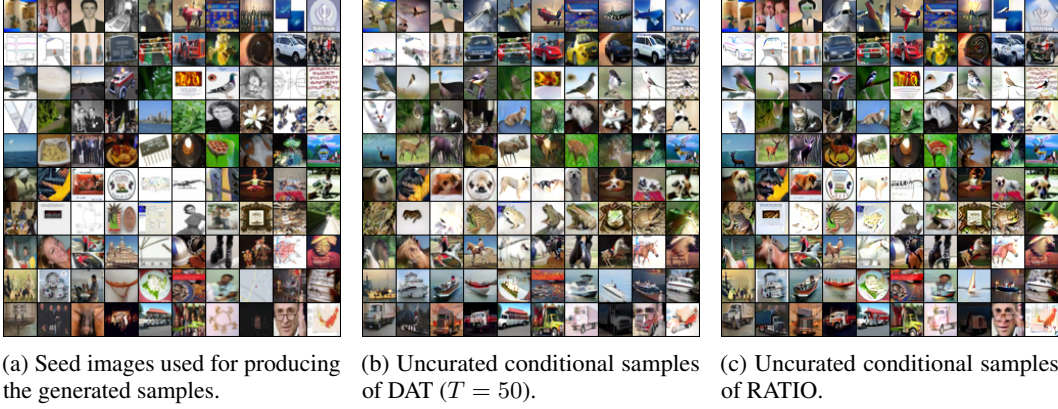


Figure 5: CIFAR-10 class-conditional generation results. Note that some samples from the RATIO baseline show potential artifacts (e.g., saturated or unnatural colors) possibly linked to the aggressive AutoAugment policy used for model training.

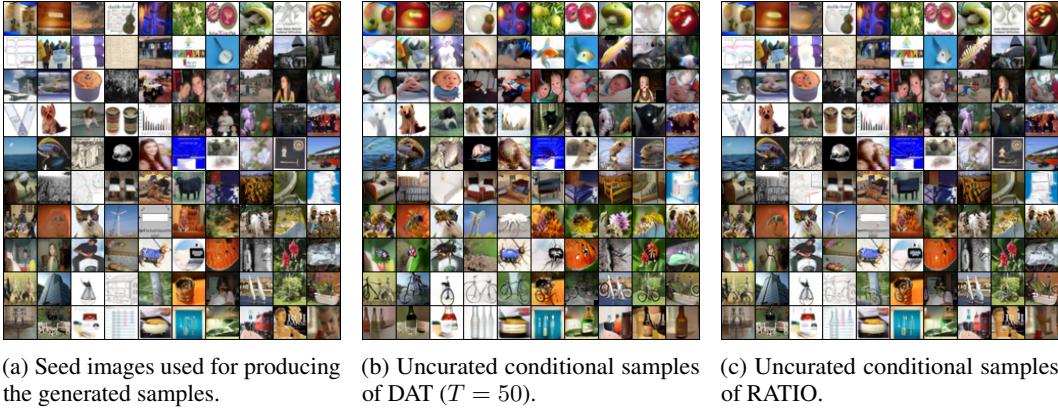


Figure 6: CIFAR-100 conditional generation results.

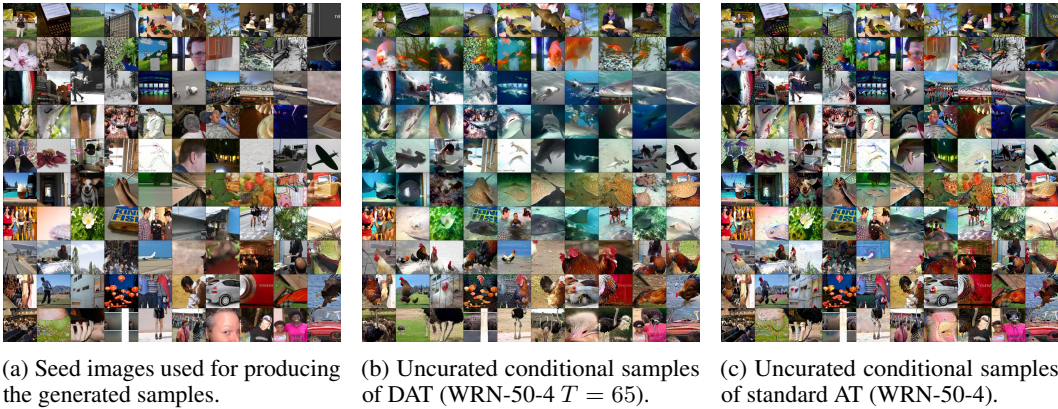


Figure 7: ImageNet class-conditional generation results for the first 10 classes: tench, goldfish, great white shark, tiger shark, hammerhead, electric ray, stingray, cock, hen, ostrich (images are in 256×256 resolution).

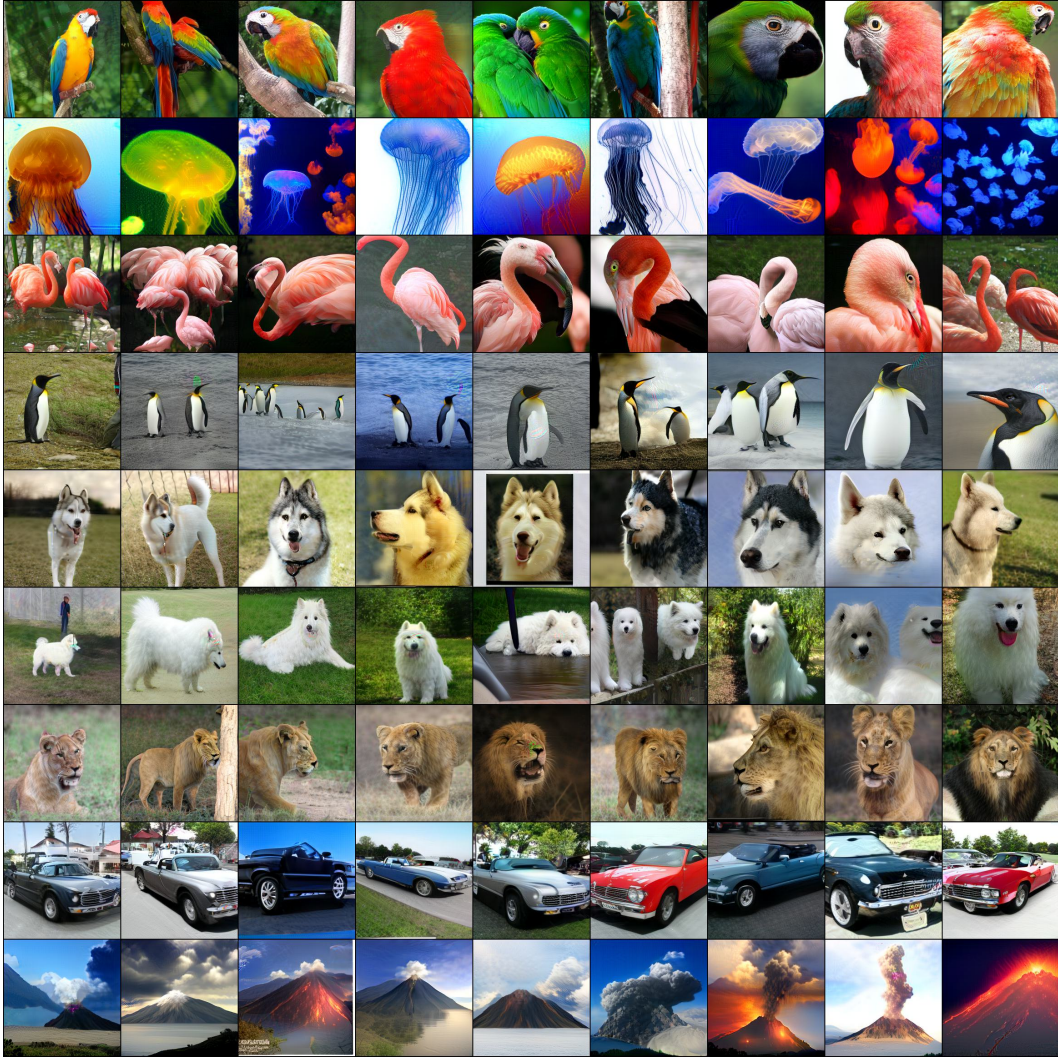


Figure 8: Selected ImageNet conditional generation results for class 88 (macaw), 107 (jellyfish), 130 (flamingo), 145 (king penguin), 248 (husky), 258 (Samoyed), 291 (lion), 511 (convertible), and 980 (volcano). Results are generated with DAT ConvNeXt-L-CvSt at 256×256

A.11 Variability of DAT performance across datasets

Table 16: Mean and standard deviation of DAT performance across datasets, computed over five independent runs with different random seeds. We observed zero divergences across all runs.

Dataset	Acc% \uparrow	Robust Acc% \uparrow	IS \uparrow	FID \downarrow
CIFAR-10 (WRN-34-10, $T = 40$)	91.92 ± 0.09	75.75 ± 0.07	9.92 ± 0.05	9.12 ± 0.05
CIFAR-100 (WRN-34-10, $T = 45$, LR=0.009)	65.76 ± 0.75	45.94 ± 0.48	10.99 ± 0.29	10.73 ± 0.25
ImageNet 256 \times 256 (ResNet-50, $T = 15$)	61.31 ± 0.16	39.96 ± 0.41	322.65 ± 2.28	6.87 ± 0.05

A.12 Training curves

We present the stage 2 training curves to illustrate the training dynamics.

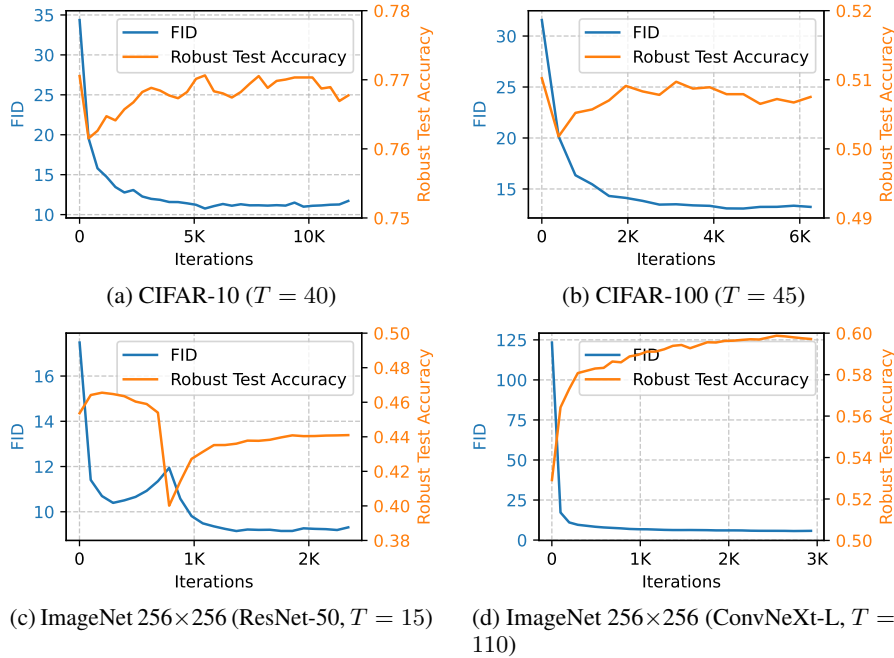


Figure 9: Training curves from Stage 2 joint training demonstrating substantial FID score improvements while preserving Stage 1 robust test accuracy (evaluated via PGD attacks; FID measured using 10K generated samples).

A.13 R_1 gradient curve

We empirically validate that adversarial training provides implicit R_1 regularization by tracking the R_1 gradient penalty during Stage 2 joint training. The R_1 regularization term measures the squared L_2 norm of the gradient of the true class logit with respect to the input (as defined in Section A.2):

$$\mathcal{L}_{R_1} = \mathbb{E}_{(x,y) \sim p_{\text{data}}} \left[\|\nabla_x f_y(x)\|_2^2 \right] \quad (25)$$

Figure 10 shows R_1 gradient norms (log scale) for ImageNet 256 \times 256 (ResNet-50, $T = 15$) training under two settings: (1) adversarial training on the discriminative loss ($\mathcal{L}_{\text{AT-CE}}$), and (2) standard training on the discriminative loss. The adversarial training curve remains bounded and stable throughout training. In contrast, the standard training curve gradually increases during early training before experiencing significant gradient growth in later stages.

This empirical observation validates the mathematical analysis in Section A.2, confirming that adversarial training inherently maintains bounded R_1 gradients equivalent to explicit R_1 regulariza-

tion. The evidence demonstrates that adversarial training’s implicit regularization suffices for stable energy-based model training.

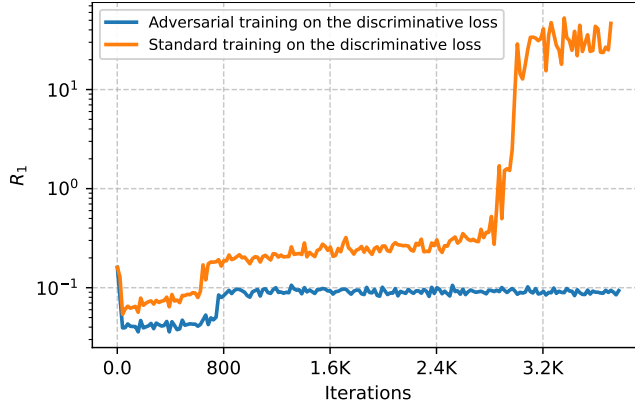


Figure 10: R_1 gradient norm during Stage 2 joint training on ImageNet 256×256 (ResNet-50, $T = 15$). Y-axis is in log scale.

A.14 Computational cost analysis

We analyze the computational costs of DAT, including training overhead, absolute training times, and inference efficiency compared to diffusion models and GANs.

Training overhead. We analyze the computational overhead of our two-stage training relative to standard adversarial training. Let E_1 and E_2 denote the number of epochs for stage 1 and stage 2, respectively, and let B denote the batch size for in-distribution samples. We measure computational cost in FLOPs, accounting for the fact that: (1) a forward pass costs 1 FLOP unit, (2) a PGD backward pass (computing ∇_x only) costs 1 FLOP unit, and (3) a training backward pass (computing both ∇_x and ∇_w) costs 2 FLOP units.

Stage 1 performs per iteration: K PGD steps (each requiring 1 forward + 1 backward w.r.t. input = 2 FLOPs) on B samples, plus one forward pass (1 FLOP) and one training backward pass (2 FLOPs) on B adversarial samples for loss computation and parameter update, totaling $(2K + 3)B$ FLOPs. Stage 2 performs per iteration: (1) K PGD steps on B in-distribution samples for $\mathcal{L}_{\text{AT-CE}}$ ($2K$ FLOPs), (2) T PGD steps on B OOD samples for \mathcal{L}_{BCE} ($2T$ FLOPs), and (3) one forward pass (3 FLOPs) and one training backward pass (6 FLOPs) on $3B$ samples (B adversarial in-distribution, B adversarial OOD, and B clean in-distribution) for combined loss computation and parameter update, totaling $(2K + 2T + 9)B$ FLOPs. This gives a per-iteration cost ratio of $(2K + 2T + 9)/(2K + 3)$ for stage 2. The total training cost relative to standard AT (which trains for E_1 epochs) is:

$$\text{Overhead} = \frac{E_1 + E_2 \cdot (2K + 2T + 9)/(2K + 3)}{E_1} = 1 + \frac{E_2}{E_1} \cdot \frac{2K + 2T + 9}{2K + 3} \quad (26)$$

Note that this formula assumes constant K and T values throughout training. In practice, we use curriculum learning where T gradually increases from a small initial value to its final value, which reduces the actual training cost. Therefore, the overhead computed above provides an upper bound on the actual computational cost.

Table 17 reports the training overhead for all our configurations, calculated using the formula above with parameters from Section A.4.1. Figure 11 visualizes the breakdown of training costs. The results show modest overhead across all settings: $1.41\text{-}1.56\times$ for CIFAR datasets and $1.05\text{-}1.36\times$ for ImageNet. Despite stage 2’s higher per-iteration cost, its short duration (especially for ImageNet with less than 1 epoch for most configurations) results in minimal additional computational cost, demonstrating that high-quality joint discriminative-generative modeling can be achieved efficiently.

Absolute training time. Table 17 reports Stage 2 effective training times (excluding FID/accuracy evaluation) on the actual hardware used (AMD Instinct MI210, MI250, and MI300 accelerators). For baseline models originally reported in V100-days (Rombach et al., 2022), we convert to MI300-hours

using benchmark-based performance ratios: MI300 is $1.3\times$ faster than H100 (AMD, 2024), and H100 is $5.69\times$ faster than V100 (Lambda Labs, 2024), yielding $\text{MI300/V100} = 7.40\times$. Our ImageNet 256×256 ConvNeXt-L Stage 2 training takes 20 hours on $8\times$ MI300, which is $\sim 5\times$ faster than LDM-4-G (110 hours on $8\times$ MI300 equivalent, 271 V100-days).

Inference efficiency. For classification, DAT requires only a single forward pass, identical to standard classifiers. For generation, our models require significantly fewer sampling steps (13-36 steps) compared to diffusion models (250 steps). Table 17 reports the generation throughput, showing $\sim 5\times$ higher throughput than LDM-4-G while achieving better FID.

Table 17: Computational cost and performance metrics of DAT models. Training overhead is computed relative to standard AT using Eq. 26. Stage 2 training times reported on actual hardware configurations (effective training time excluding FID/accuracy evaluation); baseline models converted from V100-days using $\text{MI300/V100} = 7.40\times$. Throughput measured in samples/sec on a single AMD MI300 accelerator for image generation. ADM-G and LDM-4-G throughput estimated from reported A100 measurements (Rombach et al., 2022) using relative speedups from Lambda Labs (2024) and AMD (2024).

Model	Params	Sampling steps	FID ↓	IS ↑	Training overhead	Training time (wall-clock hours)	Throughput (img/s)
<i>CIFAR-10</i>							
DAT (WRN-34-10, $T = 40$)	46M	33	9.07	9.96	$1.41\times$	10 ($4\times$ MI210, Stage 2)	39
DAT (WRN-34-10, $T = 50$)	46M	35	7.57	9.86	$1.49\times$	10 ($4\times$ MI210, Stage 2)	40
<i>CIFAR-100</i>							
DAT (WRN-34-10, $T = 45$)	46M	32	10.70	10.83	$1.52\times$	12 ($4\times$ MI210, Stage 2)	40
DAT (WRN-34-10, $T = 50$)	46M	33	9.53	11.12	$1.56\times$	12 ($4\times$ MI210, Stage 2)	39
<i>ImageNet 256×256</i>							
DAT (ResNet-50, $T = 15$)	26M	13	6.86	317.7	$1.05\times$	2.4 ($4\times$ MI210, Stage 2)	33
DAT (ResNet-50, $T = 30$)	26M	14	5.28	319.3	$1.09\times$	3.8 ($4\times$ MI210, Stage 2)	33
DAT (WRN-50-4, $T = 30$)	223M	17	6.23	341.0	$1.05\times$	4.7 ($4\times$ MI250, Stage 2)	14
DAT (WRN-50-4, $T = 65$)	223M	19	4.94	358.0	$1.09\times$	8.2 ($4\times$ MI250, Stage 2)	13
DAT (ConvNeXt-L-CvSt, $T = 110$)	198M	36	3.29	310.2	$1.36\times$	20 ($8\times$ MI300, Stage 2)	5
BigGAN-deep (Brock et al., 2018)	340M	1	6.95	203.6	—	52-104 ($8\times$ MI300-eq)	—
ADM-G (Dhariwal and Nichol, 2021)	608M	250	4.59	186.7	—	390 ($8\times$ MI300-eq)	~ 0.17
LDM-4-G (Rombach et al., 2022)	400M	250	3.60	247.7	—	110 ($8\times$ MI300-eq)	~ 0.96

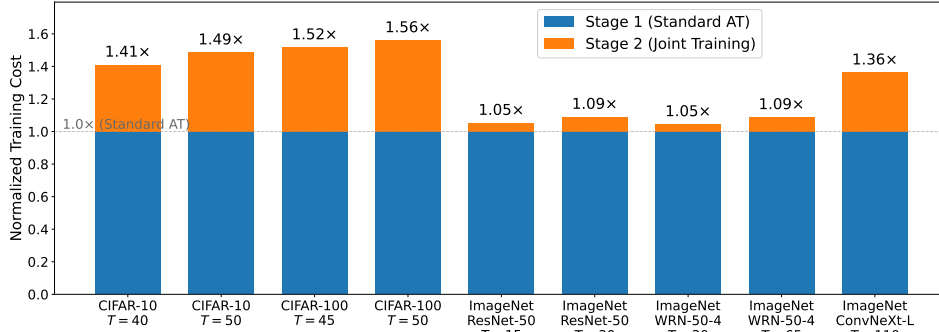


Figure 11: Training cost breakdown for all DAT configurations. The bars show the normalized training cost relative to standard adversarial training (stage 1 only, baseline $1.0\times$). Stage 1 (blue) represents standard AT, while stage 2 (orange) represents the additional cost from joint discriminative-generative training.

A.15 Formal characterization of the learned distribution

We provide a formal characterization of what distribution our BCE-with-PGD objective (Eq. 9) learns. Our analysis builds on the theoretical framework from Yin et al. (2022) (AT-EBM) and extends it to the conditional modeling setting by deriving the optimal class logits under the joint objective.

Optimal solution for class logits $f_\theta^*(x)[y]$. Following Yin et al. (2022), the BCE-with-PGD objective can be expressed as a maximin optimization problem. Let $D(x) = \sigma(-E_\theta(x))$ where $E_\theta(x) = -\log \sum_y \exp(f_\theta(x)[y])$ is the marginal energy function. For the theoretical analysis below, we assume (1) the PGD attack in Eq. 8 converges to the global minimum of $E_\theta(x)$, (2) the model has sufficient capacity, and (3) infinite training data from $p_{\text{data}}(x, y)$. Under these assumptions, minimizing $\mathcal{L}_{\text{BCE}}(\theta)$ implicitly solves:

$$\max_D \min_{p_T} U(D, p_T) = \mathbb{E}_{x \sim p_{\text{data}}(x)} [\log D(x)] + \mathbb{E}_{x \sim p_T} [\log(1 - D(x))] \quad (27)$$

where p_T represents the distribution of samples after PGD attack initialized from the auxiliary out-of-distribution dataset p_{ood} .

Under these assumptions, the optimal solution to Eq. 27 is characterized by Proposition 1 of Yin et al. (2022), which shows that at optimum $U(D^*, p_T^*) = -\log(4)$ with:

1. $D^*(x) = \frac{1}{2}$ for all $x \in \text{Supp}(p_{\text{data}}(x))$
2. $D^*(x) \leq \frac{1}{2}$ for all $x \notin \text{Supp}(p_{\text{data}}(x))$
3. p_T^* is supported on $\{x : D(x) = \frac{1}{2}\}$

where $\text{Supp}(p_{\text{data}}(x))$ denotes the support of the marginal data distribution.

The above result characterizes only the marginal energy $E_\theta(x)$, leaving the individual class logits $f_\theta(x)[y]$ underdetermined. We now derive their optimal values by incorporating the discriminative objective $\mathcal{L}_{\text{AT-CE}}$.

Proposition A.1 (Optimal class logits). *Under the assumptions stated above, at the optimal solution to the joint objective $\mathcal{L}(\theta) = \mathcal{L}_{\text{AT-CE}}(\theta) + \mathcal{L}_{\text{BCE}}(\theta)$, the class logits satisfy on the support:*

$$f_\theta^*(x)[y] = \log p_{\text{data}}(y|x) \quad \text{for all } x \in \text{Supp}(p_{\text{data}}(x)) \quad (28)$$

Proof. From the AT-EBM result above, on the support we have $D^*(x) = \sigma(-E_\theta^*(x)) = \frac{1}{2}$, which implies:

$$E_\theta^*(x) = 0 \implies -\log \sum_y \exp(f_\theta^*(x)[y]) = 0 \implies \sum_y \exp(f_\theta^*(x)[y]) = 1 \quad (29)$$

The conditional distribution is defined as:

$$p_\theta(y|x) = \frac{\exp(f_\theta(x)[y])}{\sum_{y'} \exp(f_\theta(x)[y'])} \quad (30)$$

Substituting the constraint from Eq. 29:

$$p_\theta^*(y|x) = \frac{\exp(f_\theta^*(x)[y])}{1} = \exp(f_\theta^*(x)[y]) \quad (31)$$

The cross-entropy objective $\mathcal{L}_{\text{AT-CE}}$ minimizes $-\log p_\theta(y|x)$ over $(x, y) \sim p_{\text{data}}(x, y)$, which at optimality yields $p_\theta^*(y|x) = p_{\text{data}}(y|x)$. Therefore:

$$\exp(f_\theta^*(x)[y]) = p_{\text{data}}(y|x) \quad (32)$$

Taking logarithms gives Eq. 28. □

On-support behavior. Proposition A.1 implies that on the support: (1) the joint energy equals the negative conditional log-probability $E_\theta^*(x, y) = -f_\theta^*(x)[y] = -\log p_{\text{data}}(y|x)$, (2) the marginal energy is constant $E_\theta^*(x) = 0$, and (3) the marginal model distribution is uniform $p_\theta^*(x) \propto \exp(-E_\theta^*(x)) = 1$. This confirms that the model learns a *uniform distribution over the support*, not the true density $p_{\text{data}}(x)$. For datasets with deterministic labels where $p_{\text{data}}(y|x) = \delta_{y, y_{\text{true}}(x)}$, this implies $f_\theta^*(x)[y] = 0$ for the true class and $f_\theta^*(x)[y] = -\infty$ otherwise.

Off-support behavior. For $x \notin \text{Supp}(p_{\text{data}}(x))$, the optimal solution to Eq. 27 constrains $D^*(x) \leq \frac{1}{2}$, which implies $E_\theta^*(x) \geq 0$ and thus $\sum_y \exp(f_\theta^*(x)[y]) \leq 1$. Since $\mathcal{L}_{\text{AT-CE}}$ is only computed on the data support and its adversarial perturbations, the individual class logits are underdetermined for points far from the support. From the constraint $\sum_y \exp(f_\theta^*(x)[y]) \leq 1$, we have $f_\theta^*(x)[y] \leq 0$ for all classes y , and consequently $E_\theta^*(x, y) = -f_\theta^*(x)[y] \geq 0$.

Comparison. For datasets with deterministic labels, this creates a hierarchical energy structure:

- Valid pairs ($x \in \text{Supp}, y = y_{\text{true}}$): The joint energy is exactly $E_\theta^*(x, y) = 0$.
- On-support, incorrect labels ($x \in \text{Supp}, y \neq y_{\text{true}}$): The joint energy diverges to $E_\theta^*(x, y) = \infty$.
- Off-support (OOD) ($x \notin \text{Supp}, \text{any } y$): The joint energy is bounded below, $E_\theta^*(x, y) \geq 0$, but the exact value is underdetermined.

Thus, the learned energy function $E_\theta(x, y)$ enables robust classification (via $\arg \min_y E_\theta(x, y)$), generation (via minimizing $E_\theta(x, y)$ over x), and OOD detection (via thresholding $\min_y E_\theta(x, y)$).

Finite-step vs. convergent PGD. The theoretical analysis above assumes the PGD attack converges to the global minimum of $E_\theta(x)$, which leads to the maximin formulation in Eq. 27. In practice, however, we use finite-step PGD (Eq. 8), which does not explicitly solve the inner minimization problem, creating a crucial gap between theory and practice. Our experiments demonstrate that our approach achieves diverse, high-quality generation, indicating that rather than converging to energy minima, finite-step PGD exhibits sampling-like behavior: starting from different initializations in the OOD dataset, it explores different regions of the energy landscape, leading to diverse generated samples.

Summary and implications. Our formal analysis reveals that the BCE-with-PGD objective learns a fundamentally different quantity than MLE-based methods. While MLE-based JEM theoretically learns the full density $p_\theta(x)$ with a valid partition function (though in practice short-run SGLD fails to achieve this), our approach explicitly learns the *support* of the data distribution with $E_\theta(x) = 0$ on the support. The optimal class logits $f_\theta^*(x)[y] = \log p_{\text{data}}(y|x)$ (Proposition A.1) reveal how the joint objective uniquely determines the solution on the support.

This support-based characterization has important implications. The constant marginal energy $E_\theta^*(x) = 0$ on the support means the model learns a uniform distribution over the support, theoretically discarding frequency information about the data distribution. This represents a significant theoretical limitation: the model cannot distinguish between common and rare examples within the support, and thus cannot perform density estimation tasks that require modeling relative frequencies.

Despite this limitation, the support-based formulation provides clear advantages: superior training stability compared to SGLD-based methods, robust classification, and effective OOD detection—benefits that do not require density information. Additionally, our strong empirical generation results demonstrate that the finite-step PGD dynamics discussed above act as an effective sampler, capturing density variations despite the theoretical prediction of uniformity. Overall, the support-based approach provides a practical and stable framework for joint modeling, trading full density estimation for superior training stability and strong empirical performance.

A.16 Robustness to common corruptions

To evaluate whether the joint training objective maintains robustness under distribution shift, we assess our CIFAR-10 models on CIFAR-10-C (Hendrycks and Dietterich, 2019), a benchmark testing robustness to 15 common corruption types across 5 severity levels.

As shown in Table 18, standard AT achieves a mean corruption error (mCE) of 19.63%, while DAT with $T = 40$ achieves mCE of 19.84%, and DAT with $T = 50$ achieves mCE of 21.84%. While there is a trade-off between generative quality and corruption robustness as T increases, DAT overall maintains strong corruption robustness comparable to standard AT across all corruption types.

Table 18: Robustness evaluation on CIFAR-10. We report clean accuracy, robust accuracy, and corruption robustness on CIFAR-10-C. For corruptions, we report error rate (%) averaged across 5 severity levels. mCE denotes mean corruption error across all 15 corruption types.

Metric	Standard AT	DAT ($T = 40$)	DAT ($T = 50$)
<i>Noise corruptions (error %)</i>			
Gaussian noise	21.30	20.52	20.63
Shot noise	17.14	16.36	16.86
Impulse noise	23.80	23.54	24.72
<i>Blur corruptions (error %)</i>			
Defocus blur	11.08	11.69	13.13
Glass blur	15.38	14.74	17.06
Motion blur	13.65	14.27	15.84
Zoom blur	11.72	12.39	13.89
<i>Weather corruptions (error %)</i>			
Snow	12.19	12.19	13.62
Frost	12.44	12.13	13.60
Fog	24.75	26.67	29.45
Brightness	8.26	8.60	9.61
<i>Digital corruptions (error %)</i>			
Contrast	33.31	32.89	36.24
Elastic transform	12.34	13.06	14.80
Pixelate	9.51	9.65	11.08
JPEG compression	9.56	9.73	11.14
Mean corruption error (mCE) ↓	19.63	19.84	21.84
Clean Acc (%) ↑	92.43	91.86	90.72
Robust Acc (%) ↑	75.73	75.66	74.65
FID ↓	28.41	9.07	7.19

A.17 L_∞ training

All our models in Tables 1 and 2 are trained with L_2 -based adversarial attacks for both the discriminative and generative components. To demonstrate that our approach generalizes to L_∞ adversarial training, we train on ImageNet 256×256 with ConvNeXt-L using L_∞ attacks: for discriminative training, we use 2-step PGD with $\epsilon = 4/255$ and step size $2/255$; for generative training, we use step size $3/255$ with $T = 110$ maximum steps. All other hyperparameters (optimizer, learning rate, weight decay, EMA, batch size) match our L_2 configuration exactly (see Table 3). FID is evaluated on samples generated using L_∞ -based PGD with 36 steps and step size 0.03 (approx. $8/255$).

Table 19 presents the results. Compared to Standard AT, our L_∞ -trained DAT model trades modest reductions in clean accuracy (76.58% vs 78.25%) and robust accuracy (57.94% vs 59.40%) for significantly superior generation quality (FID 4.11 vs 44.46, IS 320.7 vs 27.32). This demonstrates that DAT successfully achieves joint discriminative-generative modeling under L_∞ training, maintaining competitive robustness while enabling high-quality generation.

Comparing our L_∞ - and L_2 -trained DAT models shows each model specializes to its training norm, achieving superior robustness under that norm while maintaining comparable clean accuracy and generation quality. However, we observe a notable difference in visual quality: L_2 -trained models produce smooth generated images, while L_∞ -trained models exhibit substantial high-frequency noise artifacts, manifesting as a grainy appearance with scattered bright pixels. This artifact stems from the different constraint geometries— L_∞ perturbations allow independent bounded changes to each pixel, encouraging the PGD attack to exploit per-pixel variations, whereas L_2 perturbations enforce a global constraint that naturally penalizes high-frequency noise. These results confirm that our approach successfully generalizes to the L_∞ setting, though the choice of norm significantly influences the perceptual quality of generated samples despite similar FID scores.

Table 19: L_∞ and L_2 results on ImageNet 256×256 with ConvNeXt-L. Standard AT results are based on L_∞ -trained ($\epsilon = 4/255$) checkpoint from Singh et al. (2023). Both DAT models initialize from the same L_∞ -trained Stage 1 checkpoint (Singh et al., 2023) (no L_2 -trained checkpoint is available) and differ only in Stage 2 training: one uses L_∞ perturbations, the other uses L_2 perturbations. All models are evaluated under both L_∞ ($\epsilon = 4/255$) and L_2 ($\epsilon = 3.0$) adversarial attacks using AutoAttack (Croce and Hein, 2020).

Method	Training Norm	Clean Acc% \uparrow	Robust Acc (L_∞ 4/255) \uparrow	Robust Acc (L_2 3.0) \uparrow	FID \downarrow	IS \uparrow
Standard AT	L_∞	78.25	59.40	33.38	44.46	27.32
DAT ($T = 110$)	L_∞	76.58	57.94	33.40	4.11	320.7
DAT ($T = 110$)	L_2	75.73	51.90	56.40	3.29	310.2

A.18 Discriminative-generative trade-off

Our empirical analyses across multiple dimensions—varying PGD steps T (Section 4.3.1), adjusting loss weights (Section A.5.3), and modifying augmentation strategies (Section A.4.2)—reveal an inherent trade-off between generative and discriminative performance. The augmentation ablation provides insight into a potential underlying mechanism: when all other settings remain fixed and only the augmentation strategy for the generative component varies, using no augmentation achieves better FID but worse robust accuracy, while random cropping maintains similar FID while improving robustness. This sensitivity to the generative pipeline’s data distribution suggests that model representations adapt to the data used for generative modeling. The substantially lower FID of DAT compared to standard AT is consistent with the learned representations exhibiting stronger alignment with the original data distribution p_{data} than with the augmented distribution used for discriminative training. These observations suggest a tension between two objectives: the generative objective encourages representations aligned with p_{data} for high-fidelity generation, while the discriminative objective benefits from alignment with the augmented distribution for robustness. While this fundamental tension cannot be fully resolved within the current framework, the trade-off can be tuned through mechanisms such as PGD step count and loss weighting to suit different application requirements.